J. Fluid Mech. (2007), *vol.* 590, *pp.* 437–469.
doi:10.1017/S0022112007008166 Printed in the United Kingdom

High-resolution simulations of cylindrical density currents

MARIANO I. CANTERO[1]†, S. BALACHANDAR[2] AND MARCELO H. GARCIA[1]

[1]Department of Civil and Environmental Engineering, University of Illinois at Urbana-Champaign, Urbana, IL 61801, USA

[2]Department of Mechanical and Aerospace Engineering, University of Florida, Gainesville, FL 32611, USA

(Received 27 September 2006 and in revised form 3 July 2007)

Three-dimensional highly resolved simulations are presented for cylindrical density currents using the Boussinesq approximation for small density difference. Three Reynolds numbers (*Re*) are investigated (895, 3450 and 8950, which correspond to values of the Grashof number of 10^5, 1.5×10^6 and 10^7, respectively) in order to identify differences in the flow structure and dynamics. The simulations are performed using a fully de-aliased pseudospectral code that captures the complete range of time and length scales of the flow. The simulated flows present the main features observed in experiments at large *Re*. As the current develops, it transitions through different phases of spreading, namely acceleration, slumping, inertial and viscous. Soon after release the interface between light and heavy fluids rolls up forming Kelvin–Helmholtz vortices. The formation of the first vortex sets the transition between acceleration and slumping phases. Vortex formation continues only during the slumping phase and the formation of the last Kelvin–Helmholtz vortex signals the departure from the slumping phase. The coherent Kelvin–Helmholtz vortices undergo azimuthal instabilities and eventually break up into small-scale turbulence. In the case of planar currents this turbulent region extends over the entire body of the current, while in the cylindrical case it only extends to the regions of Kelvin–Helmholtz vortex breakup. The flow develops three-dimensionality right from the beginning with incipient lobes and clefts forming at the lower frontal region. These instabilities grow in size and extend to the upper part of the front. Lobes and clefts continuously merge and split and result in a complex pattern that evolves very dynamically. The wavelength of the lobes grows as the flow spreads, while the local *Re* of the flow decreases. However, the number of lobes is maintained over time. Owing to the high resolution of the simulations, we have been able to link the lobe and cleft structure to local flow patterns and vortical structures. In the near-front region and body of the current several hairpin vortices populate the flow. Laboratory experiments have been performed at the higher *Re* and compared to the simulation results showing good agreement. Movies are available with the online version of the paper.

1. Introduction

Density currents are flows driven by horizontal pressure gradients generated by the action of gravity over fluids with different density (Allen 1985; Simpson 1997). In

† Author to whom correspondence should be addressed.

many applications and laboratory experiments the current is channelized and confined to flow between parallel lateral walls. In such situations, if the viscous effect of the lateral walls can be ignored, the current moves as a statistically two-dimensional flow with a nominally planar front (planar current). There are a number of applications, such as the release of heavy gas into an open space, the collapse of an axisymmetric volcanic plume, or a point discharge into a lake or ocean, in which the density current is not channelized and is allowed to spread out over the entire horizontal plane. In such situations, the current moves as a statistically axisymmetric flow with a nominally cylindrical front (cylindrical current). Another example of a cylindrical current is a directed release where the current does not spread all around, but forms a conical planform. Density currents in such sector-shaped geometric tanks are often studied in the laboratory, as a proxy for the full cylindrical current, because of their simplicity. More examples of engineering, environmental and geological applications can be found in the books by Allen (1985) and Simpson (1997).

The dynamics of planar density currents is reasonably well understood (see for example Marino, Thomas & Linden 2005). Planar currents form a coherent front and a relatively long highly turbulent body behind the front (Cantero *et al.* 2007). As the currents spread, their planform increases linearly with front location and they pass through different phases, namely slumping, inertial and viscous (Huppert & Simpson 1980). On the other hand, as cylindrical currents spread the planform increases quadratically, which induces a faster decay of the current intensity. The concentrated vorticity at the head of the cylindrical current initially intensifies as the current flows out due to intense vortex stretching (Patterson *et al.* 2006), and eventually the currents present a highly turbulent front and a relatively shallow calm body (Cantero *et al.* 2006). Despite these fundamental differences, cylindrical currents are also thought to pass through a similar sequence of different phases of spreading as for planar currents (Huppert & Simpson 1980; Ungarish & Zemach 2005; Patterson *et al.* 2006).

Several experiments have been performed to study the dynamics and structure of planar density currents. Allen (1971) and Simpson (1972) have devoted great effort to the study of the lobe-and-cleft pattern observed at the front of density currents. Simpson & Britter (1979) studied the dynamics of the head of a gravity current. Huppert & Simpson (1980), Rottman & Simpson (1983) and more recently Marino *et al.* (2005) have studied the different phases of spreading of a current produced by the release of a fixed volume of denser fluid in a lighter ambient. García & Parsons (1996) and Parsons & García (1998) have studied the similarity of planar density currents fronts, to mention but a few.

In comparison, experimental investigation of cylindrical currents has been relatively limited. The earliest work to study the spreading rate of cylindrical currents was by Martin & Moyce (1952). Bonnecaze *et al.* (1995) analysed the spreading rate and deposition patterns of cylindrical particle-driven gravity currents. Alahyari & Longmire (1996) performed particle image velocimetry of a cylindrical gravity current and described the vortex dynamics in the early stages of the flow. Hallworth *et al.* (1996) studied experimentally the ambient fluid entrainment in two-dimensional and axisymmetric currents. Hallworth, Huppert & Ungarish (2001) studied experimentally the effect of rotation on the propagation of cylindrical currents. Recent experiments in a sector-shaped tank for varying fractional depth of release have been reported by Patterson *et al.* (2006).

A number of three-dimensional highly resolved simulations have been performed for planar gravity currents at modest Reynolds numbers (Re) (Lee & Wilhelmson 1997*a*, *b*; Härtel, Meiburg & Necker 2000*b*; Necker *et al.* 2002; Özgökmen *et al.* 2004;

Cantero *et al.* 2007). Such detailed information is missing for cylindrical currents and would be very useful. For example, linear stability analysis of a planar front of a gravity current has shown that the spanwise wavelength of the most unstable mode, which corresponds to the lobe-and-cleft pattern, will increase with decreasing *Re* (Härtel, Carlsson & Thunblom 2000*a*). Consistent with this theoretical prediction, as the planar current advances forward, its instantaneous *Re* decreases and a coarsening of the lobe-and-cleft structure is observed (Cantero *et al.* 2007). In the case of a cylindrical current, the instantaneous *Re* of the current decreases more rapidly due to the quadratic increase in planform. However, as the current flows out its circumferential length increases. An interesting question that arises is whether the number of lobe-and-cleft structures increases or decreases over time.

In this work we centre our attention on the release of a fixed cylindrical volume of homogeneous fluid in a slightly less dense environment, and on the time evolution of the resulting cylindrical current. We perform highly resolved simulations of three-dimensional cylindrical currents at three different *Re*, document the results and compare them to corresponding experimental observations.

2. Numerical formulation

We consider flows in which the density difference is small enough that the Boussinesq approximation can be adopted. With this approximation, density variations are only incorporated in the buoyancy term. The dimensionless governing equations are

$$\frac{\mathrm{D}\tilde{\boldsymbol{u}}}{\mathrm{D}\tilde{t}} = \tilde{\rho}\,\boldsymbol{e} - \nabla\tilde{p} + \frac{1}{Re}\nabla^2\tilde{\boldsymbol{u}}, \tag{2.1}$$

$$\nabla\cdot\tilde{\boldsymbol{u}} = 0, \tag{2.2}$$

$$\frac{\partial\tilde{\rho}}{\partial\tilde{t}} + \nabla\cdot(\tilde{\rho}\tilde{\boldsymbol{u}}) = \frac{1}{Sc\,Re}\nabla^2\tilde{\rho}. \tag{2.3}$$

Here $\mathrm{D}/\mathrm{D}\tilde{t}$ indicates the material derivative, $\tilde{\boldsymbol{u}}$ is the fluid velocity, $\tilde{p}$ is the pressure, $\tilde{\rho}$ is the density, and $\boldsymbol{e}$ is the unit vector pointing along the direction of gravity.

We have adopted the height of the fluid layer, H, as the length scale, and $U = \sqrt{g'H}$ as the velocity scale. Here $g' = g(\rho_1 - \rho_0)/\rho_0$, where g is the acceleration due to gravity, ρ_1 is the density of the denser fluid and ρ_0 is the density of the ambient fluid. Consequently, the time scale is H/U. The dimensionless density and pressure are given by

$$\tilde{\rho} = \frac{\rho - \rho_0}{\rho_1 - \rho_0}, \qquad \tilde{p} = \frac{p}{\rho_0 U^2}. \tag{2.4}$$

The two dimensionless numbers in equations (2.1)–(2.3) are, respectively, the Reynolds and Schmidt numbers, defined as

$$Re = \frac{UH}{\nu} = \frac{\sqrt{g'H^3}}{\nu} \qquad \text{and} \qquad Sc = \frac{\nu}{\kappa}, \tag{2.5}$$

where ν is the kinematic viscosity and κ is the diffusivity of temperature or chemical species producing the density change. A cylindrical volume of height H (full depth) and radius r_0 containing the heavier fluid is released into the surrounding lighter fluid. Figure 1 shows the nomenclature used in this work and the initial setting of the flow. In this work we will concentrate on the condition $r_0 = H$.

The computational domain is a rectangular box of size $\tilde{L}_x \times \tilde{L}_y \times \tilde{L}_z$. Since the current spreads radially outward along the entire $(\tilde{x}, \tilde{y})$-plane we choose $\tilde{L}_x = \tilde{L}_y$.

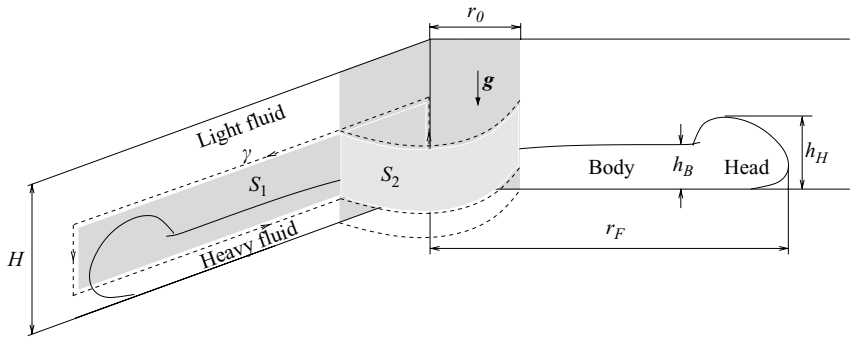

FIGURE 1. Sketch of a cylindrical density current showing the main features of the flow and nomenclature for this work.

Periodic boundary conditions are employed along the ($\tilde{x}$) and ($\tilde{y}$) directions for all variables. At the top and bottom walls no-slip and zero-gradient conditions are enforced for velocity and density, respectively. The planform of the periodic box is taken to be 15×15 in order to allow unhindered development of the current for sufficiently long time. Härtel *et al.* (2000*b*) indicated that for planar currents the interaction of the advancing front with the boundary becomes important when the front reaches within one depth scale of the boundary. This effect is expected to be less significant for cylindrical currents (see Cantero *et al.* 2006). The flow was started from rest with a minute random disturbance prescribed in the density field. The details of the initial condition can be found in Cantero *et al.* (2006). The use of a rectangular grid to solve a cylindrical problem may seem odd. However, a rectangular grid provides a uniform resolution away from the centre of the domain, thus capturing better the fine structures of the flow at the front (lobes and clefts). The governing equations are solved using a de-aliased pseudospectral code whose details can be found in Cantero *et al.* (2007).

In this work, three different Re are considered: $Re = 895$, 3450 and 8950. The corresponding Grashof numbers, defined as $Gr = g'(H/2)^3/\nu^2$ are 10^5, 1.5×10^6 and 10^7, respectively. The intermediate Re corresponds to that considered by Härtel *et al.* (2000*b*) in the planar configuration. With increasing Re the complexity of the flow increases, and this requires increased resolution. The grid resolutions employed for the three different simulations are $280 \times 280 \times 72$, $512 \times 512 \times 110$ and $880 \times 880 \times 180$ and thus they involve 5.6, 28.8 and 139.4 million grid points. The numerical resolution for each simulation was selected to have between 6 and 8 decades of decay in the energy spectrum for all the variables. The time step was selected to produce a Courant number smaller than 0.5. The simulation at $Re = 8950$ required about 1 month of continuous run on 64 processors of the new SGI Altix 3000 (put to production in April 2005 at the National Center for Supercomputing Applications (NCSA), University of Illinois at Urbana-Champaign), about 70 Gb of RAM memory to run, 600 Gb of storage for raw data, and 18 Tb (18000 Gb) of storage for visualization postprocessing by NCSA scientists.

By imposing symmetry along the $\tilde{x} = 0$ and $\tilde{y} = 0$ planes the computational domain and correspondingly the computational cost can be reduced by factor 4. Despite the increased computational cost there are advantages with the larger domain. First, if there are low-circumferential wavenumber ($k_\theta = 1$ or 2) instabilities in the propagation of the front, such instabilities can only be captured in the larger domain, without imposed symmetries. The present simulations will capture the low-wavenumber

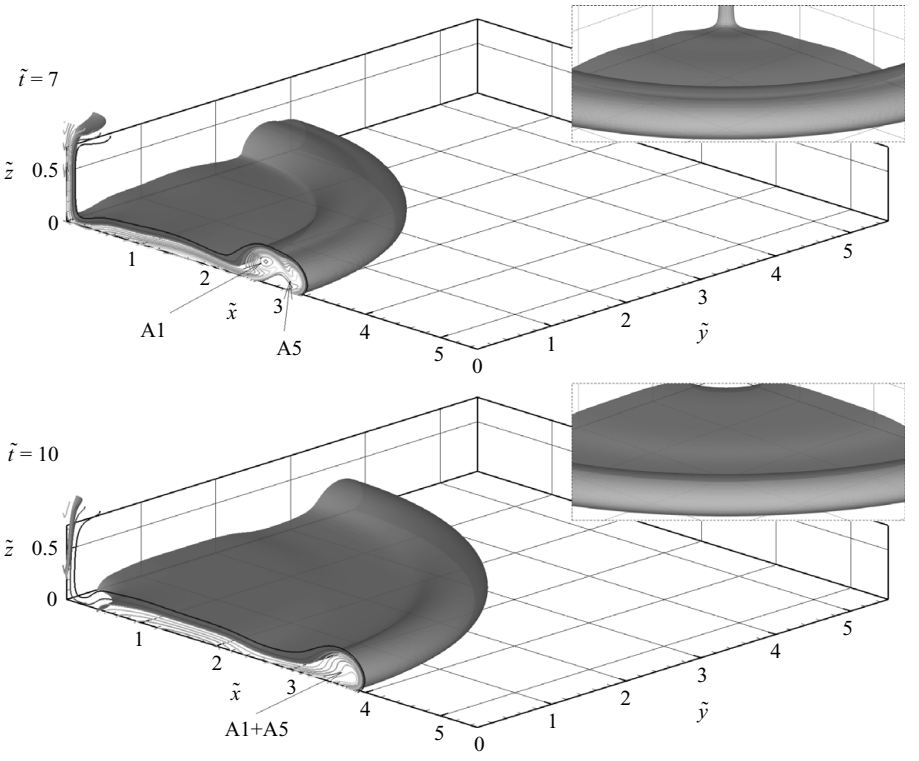

FIGURE 2. Flow visualized in one quadrant of the computational domain by isosurface of $\tilde{\rho} = 0.15$ for $Re = 895$, at two times. The head consists of two coherent anticlockwise-rotating vortex rings marked A1 and A5 on the $(\tilde{x}, \tilde{z})$-plane. The insets show a front view of the flow.

instabilities if they are present in a real system. Furthermore, we make sure that the initial perturbation in the four quadrants is dissimilar, and consequently, the evolution of the current in the four different quadrants, although statistically identical, is not exactly the same. Thus, for the higher *Re* turbulent flows, we will have data over the entire 360° degrees for more accurate extraction of the circumferentially averaged statistics.

3. Results and discussion

3.1. *Roll-up of the interface*

3.1.1. $Re = 895$

After the release of the denser fluid, an intrusive front forms. Figure 2 shows the structure of the current as visualized by a density isosurface of $\tilde{\rho} = 0.15$ for the lowest *Re* of 895. Note that the structure of the flow visualized by this isosurface does not change substantially with the choice of $\tilde{\rho}$ (see for example figure 5*a*). The figure shows only one quarter of the computational domain to allow better visualization of the flow structures. Two different dimensionless time instances are shown, $\tilde{t} = 7$ and 10. At both times a well-defined head of the current can be seen. The head initially consists of a coherent anticlockwise rotating vortex ring (marked A1 on the $\tilde{x}, \tilde{z}$ plane in figure 2) that forms first due to the roll-up of the interface shear layer between the heavy and light fluids. As the front of the current progresses radially out, the

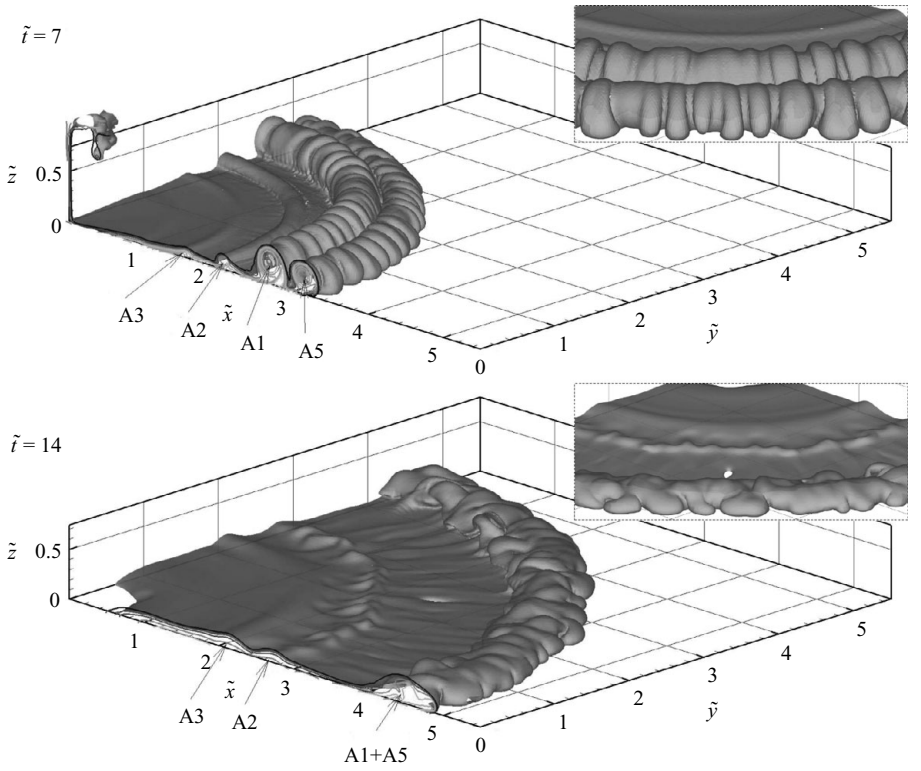

FIGURE 3. Flow visualized in one quadrant of the computational domain by isosurface of $\tilde{\rho} = 0.15$ for $Re = 3450$, at two times. Four vortex rings form, marked A1, A2, A3 and A5 on the $(\tilde{x}, \tilde{z})$-plane. For this Re, the front shows a clear pattern of lobes and clefts. The insets show a front view of the flow.

vortex ring A1 slightly lifts up above the ground and a new anticlockwise vortex ring A5 (numbering will become clear below) forms ahead of it at about $\tilde{t} \approx 5$ when the current is located at $\tilde{r} \approx 2.7$. At the earlier time of $\tilde{t} = 7$ shown in figure 2, the presence of the two different vortex rings, one behind the other, can be clearly observed and together these two vortex rings form the distinct raised head of the current. At this Re the currents remains axisymmetric at all times and the initial non-axisymmetric disturbance introduced into the flow decays away.

3.1.2. $Re = 3450$

Figure 3 shows the structure of the current at the intermediate Re of 3450. At the earlier time of $\tilde{t} = 7$ a sequence of four vortex rings can be seen. The anticlockwise vortex ring marked A1 is the first one to form at the interface. With increasing time the heavy front propagates radially out, while the light front propagates back towards the axis. Subsequent roll-up of the interface results in the formation of the vortex ring A2. In the present case, the back propagating front reaches the axis by about $\tilde{t} \approx 3$, after which the interface between light and heavy fluids increases only due to the forward propagation of the heavy front. At the same time the interface begins to roll up again to form the third vortex ring A3. These later vortices can be observed to be progressively weaker than the first one. At the earlier time of $\tilde{t} = 7$ the three vortices A1, A2 and A3 are nearly equispaced. The formation of the vortex ring A5 downstream of A1 occurs at $\tilde{t} \approx 4.5$ when the current is located at $\tilde{r} \approx 2.6$ and will be

discussed below in the context of the the higher Re case (see § 3.1.3). By about $\tilde{t} \approx 10$ the vortex rings A1 and A5 merge and form a single head of the current, which can be observed at the later time of $\tilde{t} = 14$ shown in figure 3. Also at this time, due to their faster propagation, we observe that the combined vortex ring A1+A5 is farther ahead of the weaker vortex rings A2 and A3. The dynamics of vortex propagation is explored further for the larger Re case in the next subsection.

At $Re = 3450$ the initial disturbance introduced into the flow grows over time and the flow quickly forms a lobe-and-cleft structure. The initial random disturbance introduced at the interface includes a wide range of circumferential modes. It is, however, clear from the figure that there is a preferred most amplified circumferential mode of instability. At $\tilde{t} = 7$ about 20 lobe-and-cleft structures can be observed within the quadrant that is visualized, while at $\tilde{t} = 14$ a slightly fewer number of lobe-and-cleft structures are observed. Also, at early times (not shown here) the instability was visually observed only at the head of the current, but at later times it can be observed not only at the head, but also in the subsequent vortex rings (see inset for $\tilde{t} = 7$ in figure 3). The lobes and clefts are observed to be reasonably well organized at the earlier time shown in figure 3, while at the later time their structure is less regular, suggesting the strong role of non-linearity. The height of the current is elevated only at the location of the vortex rings. In between the vortex rings the current appears to be relatively thin and calm, devoid of strong instabilities. The remnant heavy fluid observed along the axis ($\tilde{x} = \tilde{y} = 0$) and near the top boundary are artifacts of the no-slip boundary condition applied at the top boundary, but changing this to a free-slip top boundary does not alter the physics of the current to be discussed in this work.

3.1.3. $Re = 8950$

Figure 4 shows the time development of the flow structure for the highest Re of 8950. Initially, the flow evolves as a nearly axisymmetric flow in which Kelvin–Helmholtz rolls develop and form along the front and the body of the current. At $\tilde{t} = 2.7$ the nose of the current is slightly lifted away from the bottom wall and, as a consequence of the no-slip condition, a layer of light fluid penetrates below the raised nose resulting in unstable stratification. It can be observed that at this early time some incipient lobes and clefts are starting to form. However, the three-dimensionality is primarily limited to the nose of the current. A movie of the volumetric rendering of $\tilde{\rho}$ for $Re = 8950$ is available with the online version of the paper (see movie 1).

The vertical location of the nose does not depend strongly on the particular value of $\tilde{\rho}$ used to visualize the front as can be observed in figure 5(a). This figure shows circumferentially averaged density contours (as defined in equation (3.1)) for $\tilde{t} = 5.3$ and $Re = 8950$. The thick solid line indicates the contour of $\tilde{\rho} = 0.15$, the dashed lines mark the contours of $\tilde{\rho}$ between 0.01 and 0.35, and the dotted lines capture the contours of $\tilde{\rho} = 0.5$ and 0.65. Figure 5(b) shows the streamline pattern of the circumferentially-averaged velocity field at the front of the current for the same conditions as figure 5(a). The flow direction in a frame of reference moving with the front is indicated by arrows. The front of the current shows strong recirculation and the stagnation point of zero shear stress on the bottom wall is marked. It is clear that the location of the stagnation streamline does not coincide with the nose of the current. Similar results have been reported by Härtel *et al.* (2000*b*) for planar currents.

The roll-up process of the interface can be better observed from a plot of the circumferentially averaged quantities. For any flow variable f, its circumferential

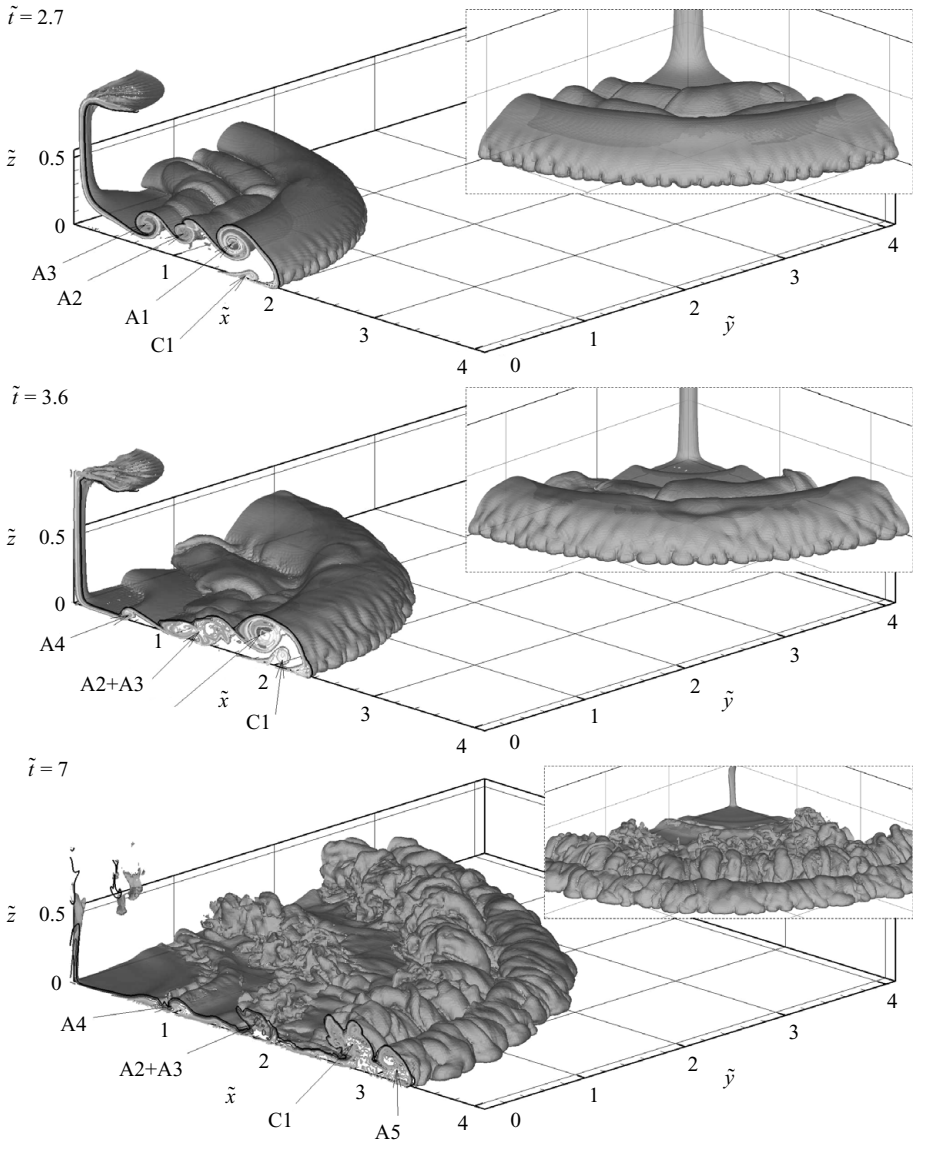

FIGURE 4. For caption, see facing page.

average is computed as

$$\bar{f}(\tilde{r}, \tilde{z}) = \frac{1}{2\pi} \int_0^{2\pi} f(\tilde{r}, \theta, \tilde{z})\, \mathrm{d}\theta. \tag{3.1}$$

In figure 6 circumferentially averaged velocity vector plots are presented at several time instances. To allow better visualization of the rolled-up vortices, the front velocity has been subtracted from the circumferentially averaged velocity field, which is plotted together with contours of circumferentially-averaged density. The interface between the heavy and light fluids is taken to be marked by $\tilde{\rho} = 0.15$. At the earliest time shown ($\tilde{t} = 1.77$), only the incipient roll-up of the anticlockwise vortex ring A1 can be seen. By $\tilde{t} = 2.7$ the back propagating front has almost reached the axis and, in

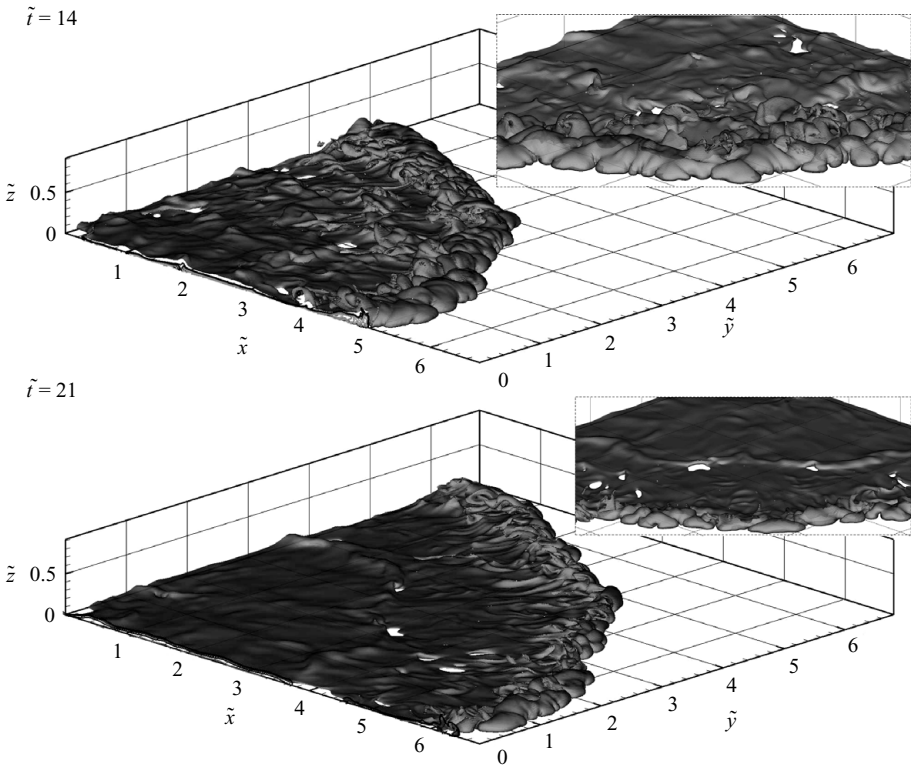

FIGURE 4. Flow visualized in one quadrant of the computational domain by isosurface of $\tilde{\rho} = 0.15$ for $Re = 8950$, at five times. Five vortex rings develop A1, A2, A3, A4 and A5 on the $(\tilde{x}, \tilde{z})$-plane. Three-dimensionality develops and destabilizes the vortex rings in the azimuthal direction which break up to smaller scale turbulence. Eventually, the turbulence decays and the body of the current becomes a calm region where most of the flow appears as interface waves. For this *Re*, the front instabilities of the initial condition grow very rapidly with time and form a pattern of lobes and clefts. The insets show a front view of the flow. See movie 1 available with the online version of the paper.

addition to the initial vortex ring A1, two additional anticlockwise vortex rings A2 and A3 can be observed upstream (see also figure 4). Also, as a consequence of the bottom no-slip boundary condition, the strong anticlockwise vortex ring A1 results in the formation of a clockwise-rotating vortex ring C1 closer to the bottom wall. At $\tilde{t} = 3.54$ the pair of vortex rings A1 and C1 form the head of the current. Vortex rings A2 and A3 have merged and have resulted in the formation of the clockwise vortex ring C2. A new rolled-up anticlockwise vortex A4 and the associated clockwise vortex ring C3 can be seen as well. The resulting vortex ring structure and the interface can be verified in figure 4. The presence of counter-rotating vortices has been observed in cylindrical gravity currents in the experiments of Alahyari & Longmire (1996).

Figure 7 shows the near-bed ($\tilde{z} = 0.017$) circumferentially-averaged radial pressure gradient ($\mathrm{d}\overline{p}/\mathrm{d}\tilde{r}$) for the case of $Re = 8950$ at $\tilde{t} = 3.54$. At this time, three regions of adverse pressure gradient ($\mathrm{d}\overline{p}/\mathrm{d}\tilde{r} > 0$) can be observed with peaks at 2.14, 1.27 and 0.63, which correspond very well with the location of the clockwise-rotating vortices C1, C2 and C3, respectively (compare to the frame for $\tilde{t} = 3.54$ in figure 6). These local adverse pressure gradients induce local boundary layer separation and the formation of the clockwise-rotating vortices as postulated by Alahyari & Longmire (1996).

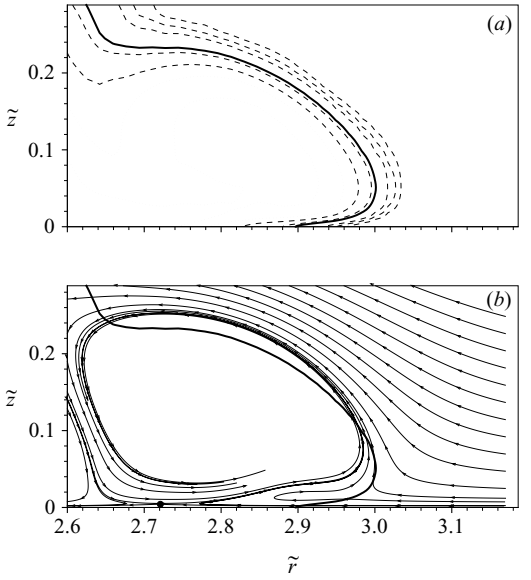

FIGURE 5. (*a*) Circumferentially averaged density contours at the front of the current for $\tilde{t} = 5.3$ and $Re = 8950$. The thick solid line indicates the contour of $\tilde{\rho} = 0.15$. The contours of $\tilde{\rho}$ between 0.01 and 0.35 are indicated by dashed lines and the contours of $\tilde{\rho} = 0.5$ and 0.65 by dotted lines. Observe that the shape of the front as indicated by contours of $\tilde{\rho}$ does not depend significantly on the particular value as long as it is in the range between 0.01 and 0.35. (*b*) Streamlines of the circumferentially averaged velocity field at the front of the current for the same flow as (*a*). The stagnation point of zero shear stress on the bottom wall is marked by a black dot. It is clear that the location of the stagnation streamline does not coincide with the nose of the current.

By $\tilde{t} = 4.67$ the vortex ring C1 has lifted the dominant vortex ring A1 further away from the bottom wall, lowering the outward propagation velocity of this structure. The front thus advances faster than the vortex ring A1 and results in the formation of a new anticlockwise vortex ring A5, downstream of A1. For this *Re* the formation of A5 occurs at $\tilde{t} \approx 4.25$ when the current is located at $\tilde{r} \approx 2.6$. This mechanism is the cause of the vortex ring marked A5 in the two lower *Re* cases as well. The azimuthal stretching of the vortices has a stabilizing effect and the coherence of the Kelvin–Helmholtz vortices is maintained until $\tilde{t} \approx 4.5$ when the current is located at $\tilde{r} \approx 2.7$. At this time instabilities grow and destabilize the Kelvin–Helmholtz rings A1, A2+A3 and A4 which eventually break up to smaller scale turbulent structures. As will be shown later, this time corresponds to the departure of the current from the slumping phase. The location of the front at the time of the transition is in good agreement with the findings of Patterson *et al.* (2006).

By $\tilde{t} = 7$ in figure 4, the vortex rings have lost their azimuthal coherence and present a wide range of scales. Also a fully developed pattern of lobes-and clefts can be observed at the front. At $\tilde{t} = 21$ only A5 that forms the front of the current and the remnant of the original vortex ring A1 can be observed. Despite the decay of the vortex rings, the lobe-and-cleft pattern is still present. The level of turbulence has decayed substantially and only the front of the current presents some vortical structures. The body of the current has become a relatively calm region, where most of the flow features appear as interfacial undulations.

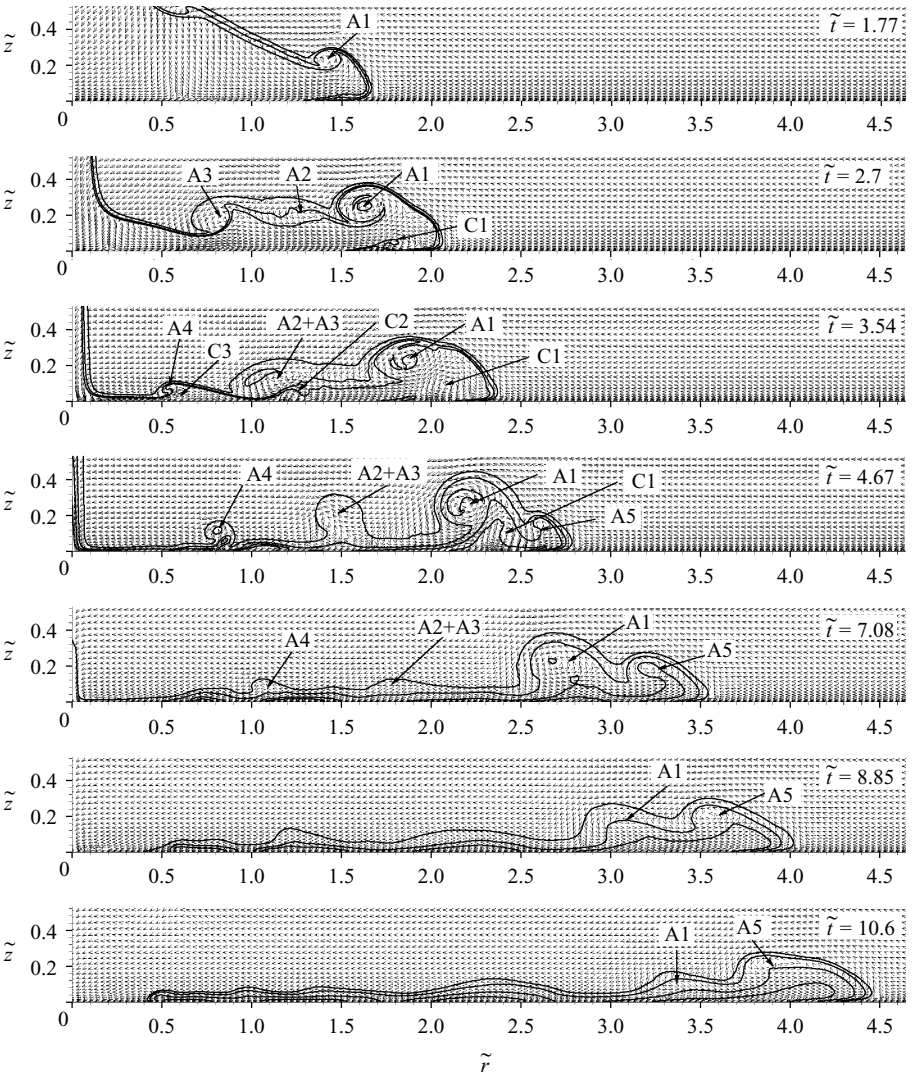

FIGURE 6. Flow field visualized by circumferentially averaged velocity vectors. To allow better vortex visualization, the nose velocity has been subtracted in each frame. The current interface is visualized by the contour of $\tilde{\rho} = 0.15$ (outer contour). Density contours are also shown to help visualize the current structure.

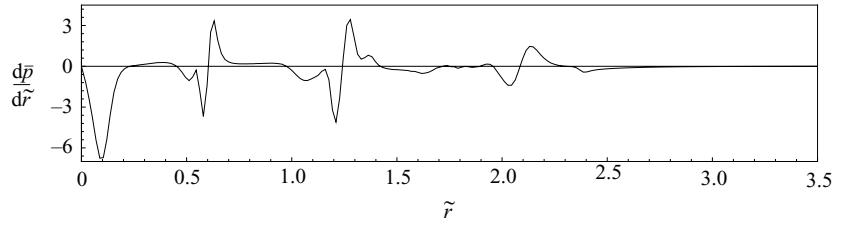

FIGURE 7. Near-bed ($\tilde{z} = 0.017$) mean radial pressure gradient for $Re = 8950$ at $\tilde{t} = 3.54$. The locations of the peaks are 2.14, 1.27 and 0.63, which correspond very well with the location of the clockwise-rotating vortices C1, C2 and C3, respectively. Compare to the location of the front and centre of the vortices in the frame for $\tilde{t} = 3.54$ in figure 6.

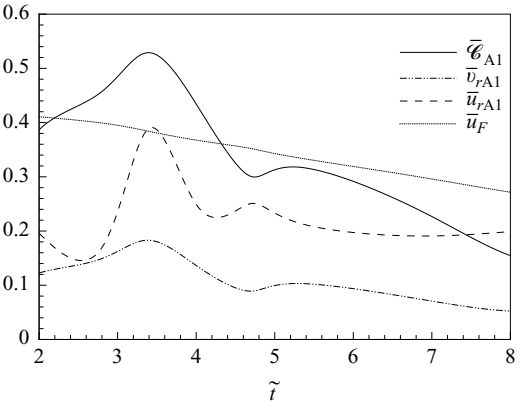

FIGURE 8. Propagation velocity of vortex ring A1 for $Re = 8950$. Solid line: circulation ($\overline{\mathscr{C}}_{A1}$), dash-dot line: self-induced velocity ($\overline{v}_{rA1}$), dashed line: radial velocity at the vortex ring core ($\overline{u}_{rA1}$), and dotted line: front velocity ($\overline{u}_F$).

3.2. *Self-induced motion of the vortex rings*

An isolated vortex ring has a propagation velocity due to self-induced motion, whose magnitude depends on the circulation of the vortex cross-section and the diameter of the ring. In the present case this self-induced motion will tend to propel the anticlockwise-rotating vortex rings towards the wall, and the clockwise-rotating vortex rings away from the wall. The magnitude of this self-induced motion is quite weak and can be ignored since the diameter of the rings is much larger than the diameter of the vortex cross-section. In other words, the curvature of the vortex rings does not play a major role.

A more significant effect arises from the interaction of the vortex rings with the wall, whose inviscid effect can be taken into account through image vortex rings. The image of an anticlockwise-rotating vortex ring across the bottom wall is a clockwise-rotating vortex ring whose interaction will tend to induce an outward radial motion. In contrast, the interaction of a clockwise-rotating vortex ring with the wall will tend to move it radially inwards. The cross-section of the vortex rings can be approximated as a Burgers vortex with a Gaussian vorticity distribution (Wu, Ma & Zhou 2006), from which the size and circulation of the vortex cross-section can be evaluated. Figure 8 shows the time evolution of circulation of the anticlockwise vortex A1, $\overline{C}_{A1}$ (solid line). The vortex circulation initially increases due to azimuthal vortex stretching (see § 3.4), but begins to weaken after $\tilde{t} > 3.4$, with an brief period of small intensification around $\tilde{t} \approx 5.2$. The corresponding size of the vortex cross-section remains approximately 0.08 dimensionless units over this period.

Assuming the vortex ring to be a line vortex, a crude estimation of the radial induced velocity from the image vortex can be obtained as $\overline{v}_{rA1} = \overline{\mathscr{C}}_{A1}/(4\pi\tilde{z}_{A1})$, where $\tilde{z}_{A1}$ is the vertical location of the vortex ring A1 core above the bottom wall. This induced radial outward velocity is also shown in figure 8 with a dash-dot-dot line. The induced velocity approximately follows the time evolution of circulation, and the differences are due to time variation in the vertical location of the vortex ring above the wall, as can be observed in figure 6. Figure 8 also presents the actual radial velocity at the vortex ring core, $\overline{u}_{rA1}$ (dashed line), and the front velocity of the current, $\overline{u}_F$ (dotted line). In general, $\overline{u}_{rA1}$ is lower than $\overline{u}_F$. As will shown later in § 3.8, the height of the current is typically larger at the vortex ring locations and as a

result the local propagation velocity is lower. Note that the propagation of a density current is due to lateral pressure difference arising from density stratification. The low dynamic pressure associated with a coherent vortex core reduces this lateral pressure gradient and lowers the local propagation velocity. Interestingly, at about $\tilde{t} \approx 3.5$ when the vortex ring A1 has reached its peak intensity, $\overline{u}_{r\mathrm{A1}}$ increases and is slightly larger than $\overline{u}_F$, which signifies the potential role of induced vortex motion. The trajectories of the vortices can be observe in a movie of the circumferentially-averaged density field available with the online version of the paper (see movie 2).

The estimated vortex velocity $\overline{v}_{r\mathrm{A1}}$ shown in figure 8 is likely to be overestimated. The estimation above ignores the presence of the top wall. For the present case of a vortex ring between two parallel walls a system of images must be considered. The effect of the top wall is to oppose the effect of the bottom wall and reduce the self-induced radial velocity. In figure 6 it can be seen that the vortices are typically located closer to the bottom wall ($z < 0.3$) and thus the effect of the bottom wall can be expected to be more than twice as strong as the top wall effect. The viscous effect of the walls needs to be accounted for as well. Furthermore, the vortex rings are not in isolation, the clockwise and anticlockwise vortex rings strongly interact among each other. Despite these complexities, it is clear that self- and mutual interactions between the vortex rings are an important ingredient, but this does not fully account for their radial propagation.

3.3. *Interface circulation estimate*

The roll-up of the flow into coherent vortex rings is clearly associated with vorticity at the interface. This process can be quantified by the integral of the azimuthal component of vorticity in an area surrounding the interface (the shaded region S_1 in figure 1 for example). This is directly related to the circulation at the interface, Γ_θ, as given by

$$\Gamma_\theta = \oint_\gamma \boldsymbol{u} \cdot \mathrm{d}\boldsymbol{s} = \int_S \boldsymbol{\omega} \cdot \mathrm{d}\boldsymbol{S}, \tag{3.2}$$

where $\boldsymbol{\omega} = \nabla \times \boldsymbol{u}$ is the vorticity and the line integral is over the path γ surrounding the surface S (marked by the dashed line and arrows in figure 1).

Figure 9(*a*) shows the evolution of the circumferentially averaged interface circulation, $\overline{\Gamma}_\theta$, for the case of $Re = 8950$. At this higher Re the viscous effects are reduced and attention can be focused on the effect of vortex stretching and baroclinic production. The integral is taken through a path line surrounding the interface with vertical bounds $\tilde{z} = 0.02$ and $\tilde{z} = 0.98$ to reduce the influence of top and bottom boundary layers. The horizontal bounds are taken to be $\tilde{r} = 0.19$ and $\tilde{r} = 7.5$ to avoid complexity in the vicinity of $\tilde{r} = 0$. This path is indicated in figure 9(*b*) by a thick long dashed line. The vertical and horizontal bounds of the contour were selected by inspection of the solution at several time instances and the behaviour of $\overline{\Gamma}_\theta$ was checked to be insensitive to these particular values as long as the contour encompasses the interface and avoids the boundary layers at the top and bottom walls and the region close to the axis. Circulation is observed to increase linearly with time until about $\tilde{t} \approx 2.3$. This period corresponds well with the formation of the vortex rings A1, A2 and A3 at the interface (see figure 6). Then, $\overline{\Gamma}_\theta$ reaches a nearly stationary value and beyond $\tilde{t} \approx 3.6$ it follows a monotonic decay.

A rough estimation of circulation at the interface can be made based on the front velocity. The jump in the circumferentially averaged radial velocity across the interface between the light and heavy fluids is proportional to the velocity of the propagating

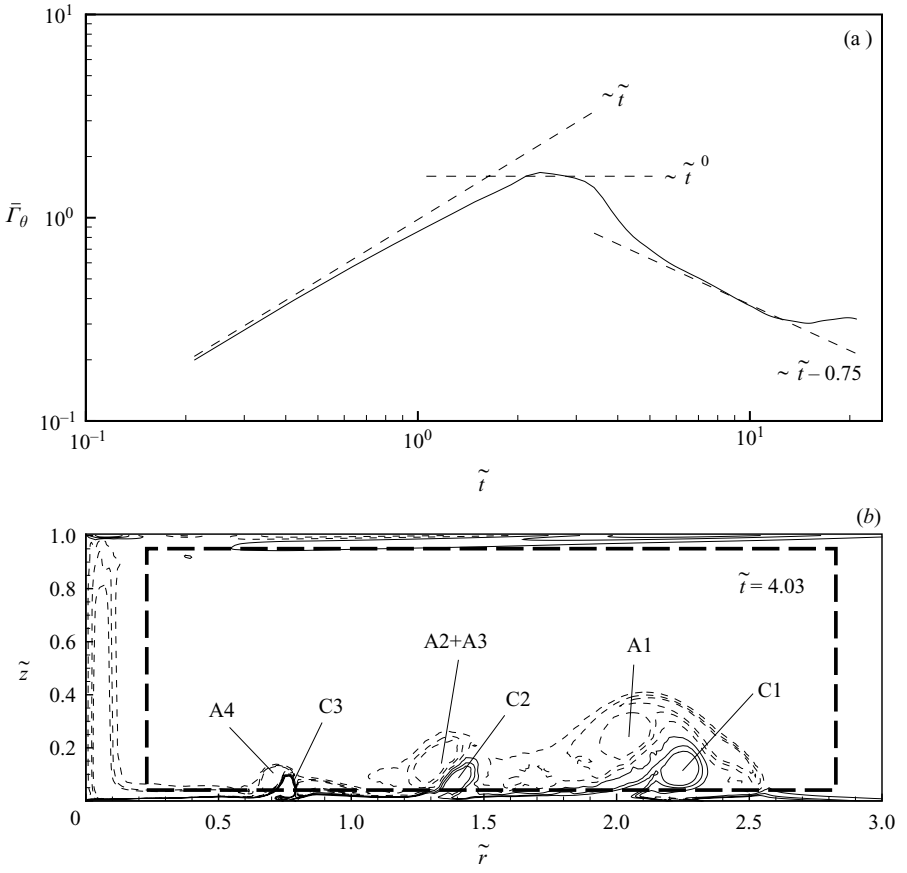

FIGURE 9. (*a*) Time evolution of $\overline{\Gamma}_\theta$ (solid line) for $Re = 8950$, together with the three scaling laws (dashed lines) $\overline{\Gamma}_\theta \sim \tilde{t}^{2\beta+1}$ for $\beta = 0, -1/2$ and $-7/8$. (*b*) Vorticity contours for $Re = 8950$ at $\tilde{t} = 4.03$. Solid lines shows negative vorticity contours corresponding to clockwise-rotating vortices (C1, C2 and C3), and dashed lines indicate positive vorticity corresponding to anticlockwise-rotating vortices (A1, A2+A3 and A4). The long dashed thick line indicates the path over which circulation is computed.

heavy front, $\overline{u}_F$. The constant of proportionality is 1.0 for a deeply submerged current and is larger for a thicker current. Nevertheless, the net circulation at the interface can be estimated as

$$\overline{\Gamma}_\theta \sim \overline{u}_F \bar{l}_F, \tag{3.3}$$

where $\bar{l}_F$ is the length of the current. If a $\overline{u}_F \sim \tilde{t}^{\beta}$ behaviour is assumed for the front velocity, then the interface circulation follows a power-law of the form

$$\overline{\Gamma}_\theta \sim \tilde{t}^{2\beta+1}. \tag{3.4}$$

It can be readily seen from the equation above that the net circulation at the interfaces increases with time only for $\beta > -1/2$. If the front velocity decays more rapidly (i.e. for $\beta < -1/2$), then net circulation at the interface decreases.

A cylindrical gravity current spreads in several phases (Fay 1969; Fannelop & Waldman 1971; Hoult 1972; Huppert & Simpson 1980). After a brief acceleration phase, the current moves at a near constant speed ($\beta \approx 0$) in the slumping phase.

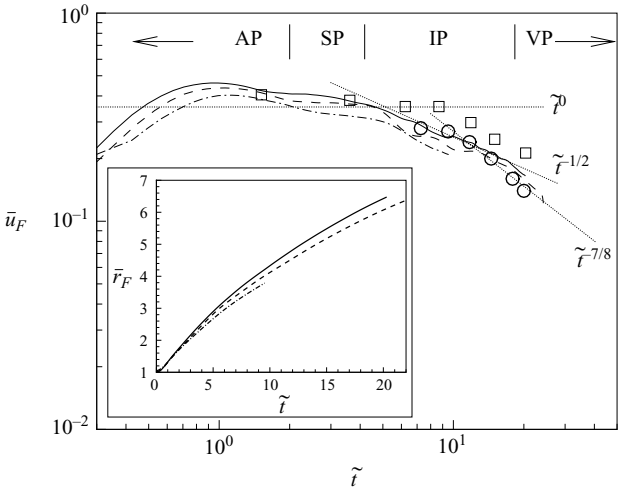

FIGURE 10. Front velocity as a function of time, in log-log scale. The transition times between phases of spreading are qualitatively indicated in the figure for $Re = 8950$. AP: acceleration phase, SP: slumping phase, IP: inertial phase, and VP: viscous phase. The inset shows front location as a function of time. Solid lines: $Re = 8950$, dashed lines: $Re = 3450$ and dashed-dot lines: $Re = 895$. Circles: data from experiment for $Re = 8950$. Squares: data from Hallworth *et al.* (2001) for $Re = 152\,000$, $r_0/H = 1.25$ and $h_0/H = 0.965$.

Then, the currents enters a self-similar phase in which the effects of flow initiation are forgotten. Provided Re is large enough to overcome viscous effects the flow first enters the self-similar inertial phase, which is characterized by a front velocity $\bar{u}_F \sim \tilde{t}^{-1/2}$ ($\beta \approx -1/2$). Finally, when viscous effects become important the current enters the viscous phase with $\bar{u}_F \sim \tilde{t}^{-7/8}$ ($\beta \approx -7/8$) (Huppert 1982). Figure 10 shows a log-log plot of velocity of the front as a function of time for the three different Re. Also shown in the figure are the $\tilde{t}^{-1/2}$ and $\tilde{t}^{-7/8}$ power-laws with corrected prefactors presented in Cantero *et al.* (2007). Although a perfect constant velocity is not observed, a brief period of slow variation in velocity is observed, which can be taken to be the slumping phase of a cylindrical current. In the inertial and viscous phases, the velocity falls off more rapidly and the computed decay in the front velocity is in reasonable agreement with what is theoretically predicted. Also shown in the figure are results from present experiments (to be described below) performed at $Re = 8950$ corresponding to the highest Re simulation and those from Hallworth *et al.* (2001). The comparison between the present simulations and experiments is very good. The experiments of Hallworth *et al.* (2001) are at a higher Re of 152 000 and in a slightly different geometric set up ($r_0/H = 1.25$ and $h_0/H = 0.965$). This difference may contribute to the slightly higher front velocity observed in their experiments.

Full-depth cylindrical currents of unit initial radius will pass through the sequence of slumping, inertial and viscous phases of spreading only when the initial Re of release is greater than 900. Less intense currents of $Re < 900$ will directly transition from the slumping to viscous phase (Cantero *et al.* 2007). The dimensionless transition time from the slumping to the self-similar inertial phase, $\tilde{t}_{SI}$, and from the self-similar inertial to the viscous phase, $\tilde{t}_{IV}$, can be estimated as

$$\tilde{t}_{SI} = \frac{0.67}{F_{c,sl}^2}, \qquad \tilde{t}_{IV} = 0.4\, Re^{1/3}, \tag{3.5}$$

respectively. Here $F_{c,sl}$ is the approximate constant dimensionless velocity of the front in the slumping phase, which takes an approximate value of 0.41 at $Re = 8950$ (Cantero *et al.* 2007). According to the above equation, for the case of $Re = 8950$ the transition times can be estimated to be $\tilde{t}_{SI} = 4$ and $\tilde{t}_{IV} = 8.3$. The estimate for $\tilde{t}_{SI}$ is in good agreement with the transition time observed in figure 10. On the other hand, the estimate for $\tilde{t}_{IV}$ is consistently larger than what is observed in figure 10.

Based on the simple scaling presented in equation (3.4), we expect circulation to increase linearly with time ($\overline{\Gamma}_\theta \sim \tilde{t}$) in the slumping phase. During the inertial phase ($\beta \approx -1/2$) circulation is expected to remain constant and finally in the viscous phase ($\beta \approx -7/8$) circulation is expected to decay as $\overline{\Gamma}_\theta \sim \tilde{t}^{-3/4}$. These power-law behaviours are shown for reference in figure 9(*a*) and the agreement with the computed circulation is quite good. However, according to the theoretical estimates, $\overline{\Gamma}_\theta$ is expected to increase linearly until $\tilde{t} \approx 4$, remain approximately constant until $\tilde{t} \approx 10$, and decay as $\overline{\Gamma}_\theta \sim \tilde{t}^{-3/4}$ from there on. As observed in figure 9(*a*), the scaling is followed but the transition times are different. The estimates are based on the assumption of a constant velocity during the slumping phase. Clearly, this is only approximately valid and may contribute to the observed difference.

In Cantero *et al.* (2007) it was observed that the formation of the first vortex ring (A1) marks the end of the rapid acceleration of the front following the initial release. We note that the formation of all new anticlockwise vortex rings happens over $\tilde{t} \lesssim 5.0$, primarily during the slumping phase. At $Re = 895$ only two vortex rings (A1 and A5) form during this period and at $Re = 3450$ and 8950 four and five vortex rings form, respectively. After $\tilde{t} \approx 5.0$, i.e. during the inertial and viscous phases, no new vortices are observed to form in any of the cases simulated. The formation of vortex A5 coincides with the transition time from the slumping phase. The number of vortex rings that form is primarily a function of both Re and the aspect ratio of the volume of release r_0/h_0, where h_0 is the initial height of the release. With increasing aspect ratio of the volume of release, the time spent in the slumping phase increases (Cantero *et al.* 2007) and during this period circulation at the interface continues to increase. With increasing Re the frequency at which the interface rolls up to form coherent vortices increases. After the formation of the last vortex ring (A5) the Kelvin–Helmholtz rolls start to destabilize in the azimuthal directions and eventually decay to concentrated regions of smaller scale turbulence.

3.4. *Vorticity dynamics*

The complex dynamics of the vortex rings is controlled by a delicate balance between production, stretching, tilting, transport and dissipation. This balance also controls the stability of the ring structure and its eventual breakup into smaller scales. Vorticity dynamics is dictated by (see for example Wu *et al.* 2006)

$$\frac{\mathrm{D}\tilde{\boldsymbol{\omega}}}{\mathrm{D}\,\tilde{t}} = \tilde{\boldsymbol{\omega}} \cdot \nabla\tilde{\boldsymbol{u}} + \nabla\tilde{\rho} \times \boldsymbol{e} + \frac{1}{Re}\nabla^2\tilde{\boldsymbol{\omega}}, \tag{3.6}$$

where the first term on the right-hand side is responsible for vortex stretching and tilting, the second term accounts for baroclinic production of vorticity and the third term represents vorticity diffusion. Here we focus on the balance of net normal vorticity across a fixed surface $\boldsymbol{s}$, which can be expressed as

$$\frac{\partial}{\partial\,\tilde{t}}\int_S \tilde{\boldsymbol{\omega}} \cdot \mathrm{d}\boldsymbol{S} = \int_S (-\tilde{\boldsymbol{u}} \cdot \nabla\tilde{\boldsymbol{\omega}}) \cdot \mathrm{d}\boldsymbol{S} + \int_S (\tilde{\boldsymbol{\omega}} \cdot \nabla\tilde{\boldsymbol{u}}) \cdot \mathrm{d}\boldsymbol{S} + \int_S (\nabla\tilde{\rho} \times \boldsymbol{e}) \cdot \mathrm{d}\boldsymbol{S} + \int_S \left(\frac{1}{Re}\nabla^2\tilde{\boldsymbol{\omega}}\right) \cdot \mathrm{d}\boldsymbol{S}. \tag{3.7}$$

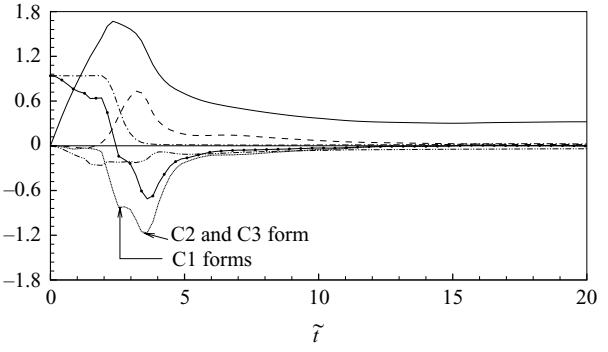

FIGURE 11. Time evolution of $\overline{\Gamma}_\theta$ (solid line), $\overline{\mathscr{A}}_\theta$ (dotted line), $\overline{\mathscr{S}}_\theta$ (dashed line), $\overline{\mathscr{B}}_\theta$ (dash-dotted line) and $\overline{\mathscr{D}}_\theta$ (dash-dotted-dotted line) for $Re = 8950$. The solid line with closed circle symbols is $\mathrm{d}\overline{\Gamma}_\theta/\mathrm{d}\tilde{t}$ (see equation (3.8)).

First we choose the surface to be a radial slice through the flow (surface S_1 in figure 1 for example). In this case $\mathrm{d}\boldsymbol{S} = \mathrm{d}S\boldsymbol{e}_\theta$ and equation (3.7) dictates the evolution of the azimuthal component of vorticity. The circumferential average can then be computed for each term to obtain

$$\frac{\mathrm{d}\overline{\Gamma}_\theta}{\mathrm{d}\tilde{t}} = \overline{\mathscr{A}}_\theta + \overline{\mathscr{S}}_\theta + \overline{\mathscr{B}}_\theta + \overline{\mathscr{D}}_\theta \tag{3.8}$$

where $\overline{\mathscr{A}}_\theta$, $\overline{\mathscr{S}}_\theta$, $\overline{\mathscr{B}}_\theta$ and $\overline{\mathscr{D}}_\theta$ are, respectively, advection, stretching and tilting, baroclinic production and diffusion of $\overline{\Gamma}_\theta$. Here we take the surface S to be the same as that bounded by the contour shown in figure 9(*b*).

Figure 11 shows the time evolution of every term in equation (3.8). The baroclinic production of azimuthal vorticity, $\overline{\mathscr{B}}_\theta$, is related to the net radial density gradient, $\partial\tilde{\rho}/\partial\tilde{r}$, within the domain of integration. We observe $\overline{\mathscr{B}}_\theta$ to be always positive and nearly constant until $\tilde{t} \approx 2$. After this time $\overline{\mathscr{B}}_\theta$ decays to nearly zero by $\tilde{t} \approx 3.6$. Thus, beyond this time positive and negative $\partial\tilde{\rho}/\partial\tilde{r}$ are in approximate balance. On the other hand, the stretching term, $\overline{\mathscr{S}}_\theta$, has a small negative value until $\tilde{t} \approx 2$. Subsequently it increases to peak at $\tilde{t} \approx 3.2$ followed by a rapid decay till $\tilde{t} \approx 5$. Between $\tilde{t} \approx 5$ and 9, $\overline{\mathscr{S}}_\theta$ maintains a small but approximately constant positive value. Afterwards it decays to negligibly small values.

The baroclinic term is the only true production term. Stretching, titling and advection mechanisms modify the vorticity distribution, but conserve circulation. Here $\overline{\mathscr{S}}_\theta$ is more than counter-balanced by $\overline{\mathscr{A}}_\theta$. A detailed inspection of the results shows that the main contribution to $\overline{\mathscr{A}}_\theta$ is the inflow of negative azimuthal vorticity (clockwise-rotating vortices) at the bottom boundary. The inflow is due to the formation and uplift of clockwise-rotating vortices C1, C2 and C3 (see also figures 4 and 6). This is clearly seen in figure 9(*b*) which shows vorticity contours for $Re = 8950$ at the time $\overline{\mathscr{A}}_\theta$ peaks, $\tilde{t} = 4.03$. Observe in figure 11 that while all the other terms tend to zero more rapidly, $\overline{\mathscr{D}}_\theta$ remains negative for an extended period. The slight increase in $\overline{\mathscr{D}}_\theta$ at $\tilde{t} < 4$ is associated with larger gradients of the azimuthal component of vorticity induced by tilting and bending of the interface vortex rings due to instability, which we explore next.

The baroclinic production is limited to only the azimuthal and radial components of vorticity, while it is only by tilting and bending of the vortex rings that the vertical component of vorticity is generated. Here we will focus on the evolution of the

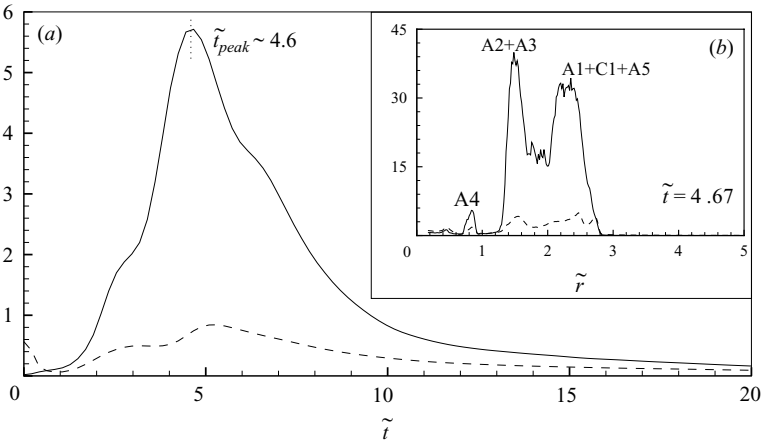

FIGURE 12. Time evolution of $\overline{\mathscr{S}}_r$ (solid line) and $\overline{\mathscr{B}}_r$ (dashed line) for $Re = 8950$. Inset radial distributions of $\tilde{\mathscr{S}}_r$ (solid line) and $\tilde{\mathscr{B}}_r$ (dashed line) for $Re = 8950$ at the time of the peak for $\overline{\mathscr{S}}_r$, $\tilde{t} \approx 4.6$. Three peaks are observed for $\tilde{\mathscr{S}}_r$ that correspond to the locations of A1+C1+A5, A2+A3 and A4. This can be verified in figure 6. The distribution of $\tilde{\mathscr{B}}_r$ is more homogeneous but also shows peaks corresponding to the vortex ring locations.

radial component, but a similar analysis can be performed for the vertical component as well. Consider equation (3.7) with the surface chosen to be a cylindrical shell with $\mathrm{d}\boldsymbol{s} = \mathrm{d}S\boldsymbol{e}_r$ (surface S_2 in figure 1 for example). In this case equation (3.7) dictates the evolution of the radial component of vorticity. The cylindrical surface S extends the entire 360° with vertical bounds $\tilde{z} = 0.02$ and $\tilde{z} = 0.98$, thus avoiding the boundary layers. The most important contributions are from the stretching and baroclinic production terms; however, the net contribution of both these stretching and baroclinic production terms is zero since negative and positive radial vorticity are produced at the same rate. A more reliable measure of the radial components of these terms is in terms of the root-mean-square (r.m.s.) values given by

$$\tilde{\mathscr{S}}_r = \sqrt{\int_S [(\tilde{\boldsymbol{\omega}} \cdot \nabla \tilde{\boldsymbol{u}}) \cdot \boldsymbol{e}_r]^2 \, \mathrm{d}S}, \qquad \tilde{\mathscr{B}}_r = \sqrt{\int_S [(\nabla \tilde{\rho} \times \boldsymbol{e}) \cdot \boldsymbol{e}_r]^2 \, \mathrm{d}S}. \tag{3.9}$$

The radial average of these quantities can be computed as

$$\overline{\mathscr{S}}_r = \frac{1}{\tilde{L}_r - 0.19} \int_{0.19}^{\tilde{L}_r} \tilde{\mathscr{S}}_r \, \mathrm{d}\tilde{r}, \qquad \overline{\mathscr{B}}_r = \frac{1}{\tilde{L}_r - 0.19} \int_{0.19}^{\tilde{L}_r} \tilde{\mathscr{B}}_r \, \mathrm{d}\tilde{r}. \tag{3.10}$$

We note that the above are not precise equivalent of $\overline{\mathscr{S}}_\theta$ and $\overline{\mathscr{B}}_\theta$, respectively, since the radial component measures r.m.s. while the azimuthal component measures the mean.

Figure 12 shows the time evolution of $\overline{\mathscr{S}}_r$ (solid line) and $\overline{\mathscr{B}}_r$ (dashed line) for the case of $Re = 8950$. The baroclinic production of radial vorticity comes from azimuthal density gradients, $\partial\tilde{\rho}/\partial\theta$, and thus in a pure axisymmetric flow there is no baroclinic production of radial vorticity. Non-zero azimuthal density gradients are supported only when axisymmetry is broken through the instability mechanism. In other words, the vortex rings must first undergo instability along the radial direction for the production terms to be active. Then, the stretching and tilting contribution to radial vorticity will be more important than baroclinic production. It can be observed in

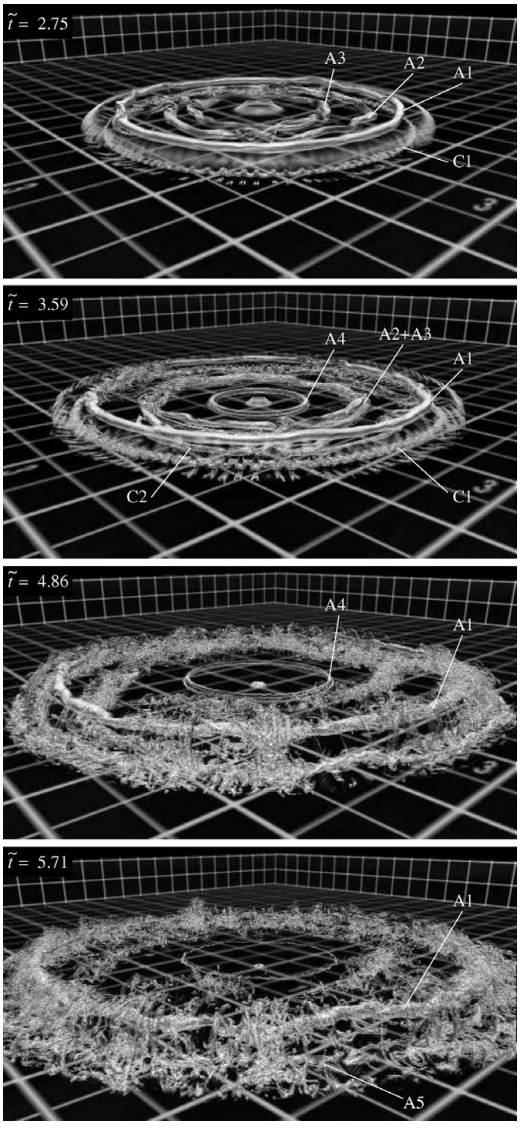

FIGURE 13. Volumetric rendering of $\tilde{\lambda}_{ci}$ for $Re = 8950$. The vortex ring structures in the flow undergo bending and tilting, and eventually break up to small-scale turbulence. See movie 3 available with the online version of the paper.

figure 12(*a*) that $\overline{\mathscr{S}}_r$ is about an order of magnitude larger than $\overline{\mathscr{B}}_r$. The peak value of $\overline{\mathscr{S}}_r$ is reached at $\tilde{t} \approx 4.6$ which is about the time at which the vortex rings destabilize and the rapid breakup starts. The inset in figure 12 shows the radial distribution of $\tilde{\mathscr{S}}_r$ (solid line) and $\tilde{\mathscr{B}}_r$ (dashed line) at $\tilde{t} = 4.67$ when $\overline{\mathscr{S}}_r$ peaks. The curve for $\tilde{\mathscr{S}}_r$ shows three clear peaks located at $\tilde{r} \approx 2.3$, 1.5 and 0.85. It can be verified in figure 6 that these peaks correspond to the locations of A1+C1+A5, A2+A3 and A4, respectively. The destabilization of the vortex rings contributes to the radial component and result in the rapid breakup of the vortex rings.

Figure 13 shows the volumetric rendering of the *swirling strength* (see also § 3.7) for the simulation at $Re = 8950$. Here the swirling strength, $\tilde{\lambda}_{ci}$, is defined as the absolute

value of the imaginary portion of the complex eigenvalues of the local velocity gradient tensor. As discussed in Zhou *et al.* (1999) and Chakraborty, Balachandar & Adrian (2005) the swirling strength provides a clean measure of the compact vortical structures of the flow. The swirling strength picks out regions of intense vorticity, but discriminates against planar shear layers, where vorticity is balanced by strain rate. In this figure the vortex rings can be clearly identified undergoing bending and tilting, which lead to the final breakup process. A movie with the volumetric rendering of $\tilde{\lambda}_{ci}$ is available with the online version of the paper (see movie 3).

The understanding of the dynamics of vortex tilting and bending by vortex stretching can be complemented by the following analysis. Consider, for example, a vortex tube located at the centre of the vortex ring A1. Let $(\boldsymbol{s}, \boldsymbol{n}, \boldsymbol{b})$ be the tangent, principal normal (pointing to the centre of curvature of the vortex tube), and bi-normal orthonormal basis vectors, respectively. Let υ and χ be the curvature and the torsion of the vortex tube, respectively, (the torsion of the vortex tube accounts for the curvature in the vertical-azimuthal plane) and $\tilde{\boldsymbol{u}} = (\tilde{u}_s, \tilde{u}_n, \tilde{u}_b)$ the velocity based on this basis. Then, the stretching term is

$$\tilde{\boldsymbol{\omega}} \cdot \nabla \tilde{\boldsymbol{u}} = \tilde{\omega} \left[\left(\frac{\partial \tilde{u}_s}{\partial s} - \tilde{u}_n \upsilon \right) \boldsymbol{s} + \left(\frac{\partial \tilde{u}_n}{\partial s} + \tilde{u}_s \upsilon - \tilde{u}_b \chi \right) \boldsymbol{n} + \left(\frac{\partial \tilde{u}_b}{\partial s} + \tilde{u}_n \chi \right) \boldsymbol{b} \right], \quad (3.11)$$

where $\tilde{\omega} = |\tilde{\boldsymbol{\omega}}|$. Consider the simplest case in which, $\tilde{u}_s = 0$, $\partial/\partial s = 0$ (no azimuthal variation), and that the vortex tube is slightly perturbed (see for example the frame for $\tilde{t} = 2.75$ in figure 13) so that the vortex tube has torsion $\chi \neq 0$. Consistent with this last assumption is to assume a small $u_b \neq 0$. In this case

$$\tilde{\boldsymbol{\omega}} \cdot \nabla \tilde{\boldsymbol{u}} = \tilde{\omega}(-\tilde{u}_n \upsilon \boldsymbol{s} - \tilde{u}_b \chi \boldsymbol{n} + \tilde{u}_n \chi \boldsymbol{b}). \quad (3.12)$$

The component along $\boldsymbol{s}$ accounts for the intensification of azimuthal vorticity, and the components along $\boldsymbol{n}$ and $\boldsymbol{b}$ account for vortex tilting. Once the vortex rings form, they undergo initially azimuthal stretching which stabilize and intensify them. After the vortex rings are slightly perturbed, vortex stretching in the radial and vertical directions produce tilting and bending starting a self-reinforced process that leads to rapid breakup of the structures (see movie 3). As it is clear from equation (3.12) this process is proportional to the magnitude of the vorticity, which is intensified by the azimuthal component of vortex stretching.

3.5. *Qualitative experiments*

For comparison, we have also performed a laboratory experiment in a rectangular tank of size $2\,\mathrm{m} \times 2\,\mathrm{m} \times 0.5\,\mathrm{m}$. At one corner of the box a quarter-cylinder of radius 0.165 m is filled with salt water of slightly higher density. The rest of the tank is filled with fresh water and the two regions are initially separated with a cylindrical lock. Both the fresh and salt water are maintained to the same height of 0.165 m and therefore here we consider a full-depth release with $r/H = 1$. The salt water is dyed with potassium permanganate in order to visualize the front as it propagates out. The present experiment can thus be considered as a cylindrical current in a 90° sector. The density difference and the height of the layer are chosen to yield $Re = 8950$, and thus the results can be directly compared to those for the simulation with the same Re. The bottom of the tank presents a smooth no-slip surface for the flow and the free surface at the top presents a slip condition. In the experiment, the heavy fluid is released in a finite amount of time (the time to lift the gate) and thus the initial condition is not exactly the same as in the simulations. Despite the differences in the experimental set-up and the numerical simulation, the results resemble each

other very closely. Figure 10 shows that the front velocity during the inertial and viscous phases from the simulations are in very good agreement with those from the experiment. Also, the lobe-and-cleft pattern is qualitatively well captured by our simulation. Figure 14 shows the lobe-and-cleft pattern from the experiment for four time instances when the front is located at approximately $\tilde{r} = 3.6$, 4.1, 4.5 and 5.0. Each frame shows the complete front (that is the 90° circular sector) of the current in the experiment. Through postprocessing of the images, the lobes and clefts could be clearly demarcated. Lobes are indicated with arrows to allow a quantitative comparison with simulation results. Note that the Sc for salt in water is 700, while the computations employ $Sc = 1$. The good agreement between numerical results and experimental observations (to be shown below) offers some justification for findings that, as long as $Sc > O(1)$, the flow and the lobe-and-cleft pattern are not very sensitive to the precise value of Sc (Härtel *et al.* 2000*b*; Cantero *et al.* 2006).

3.6. *Lobes and clefts*

The three-dimensional lobe-and-cleft structure of the advancing front can be seen in figures 3 and 4 for the larger two Reynolds number simulations considered in this paper. The azimuthal variation in front propagation continues after the initial formation of lobes and clefts and, as a result, the number and location of lobes and clefts constantly change along the front. The front of the current identified by the contour of $\tilde{\rho} = 0.015$ at the bottom boundary is plotted on the $(\tilde{x}, \tilde{y})$-plane (top view) in figure 15. The front location at several equispaced time intervals of $\Delta\tilde{t} = 0.354$ are superposed for $Re = 3450$ in frame (*a*) and for $Re = 8950$ in frame (*b*). The composite picture provides a clear view of the formation of lobes and clefts and the footprint the clefts leave on the horizontal $(\tilde{x}, \tilde{y})$-plane as the front advances over time. At the beginning (toward the centre of the figure) the front is nearly axisymmetric, but small random disturbances introduced in the initial condition quickly develop into well-formed lobe-and-cleft structures. Different instability mechanisms for the formation of the lobe-and-cleft structure of the front have been proposed in the context of planar currents (Allen 1971; Simpson 1972; Härtel *et al.* 2000*a*). These mechanisms are likely to be active and responsible for the lobe-and-cleft structure of the cylindrical currents as well. Even after they are fully formed, the speed of the current continues to vary along the circumference of the front, thus resulting in repeated splitting and merging of existing lobes-and-clefts. A complex pattern is etched by the clefts as the front advances, with repeated formation of new ones and merger between older ones, which is well captured in figure 15.

Figure 16 shows a snapshot of the near-bed flow at the front of the current for $Re = 3450$ at $\tilde{t} = 21$. The inset in the figure indicates the location of the horizontal section at $\tilde{z} = 0.04$ relative to the front where the flow is shown. The front is visualized by the density contour of $\tilde{\rho} = 0.015$ at the bottom wall (denoted by a thick solid line). The vector field shows the horizontal flow (velocity components $\tilde{u}_x$ and $\tilde{u}_y$) in a fixed frame of reference, and the contour lines show the vertical flow (solid line: positive $\tilde{u}_z$, and dashed line: negative $\tilde{u}_z$). The vector field shows clearly that the horizontal flow in the clefts is slower than in the lobes, and that there is an azimuthal component that is directed from the centre of the lobes into the clefts. This flow pattern had been postulated by Allen (1985). The contours of vertical velocity show upward flow at the clefts and downward flow at the lobes. The composition of these results shows that each lobe has a pair of counter-rotating vortices as originally postulated by Allen (1985). Some evidence of vortical activity at the front of the current can be seen in figures 13 and 19 (to be discussed in detail in § 3.7).

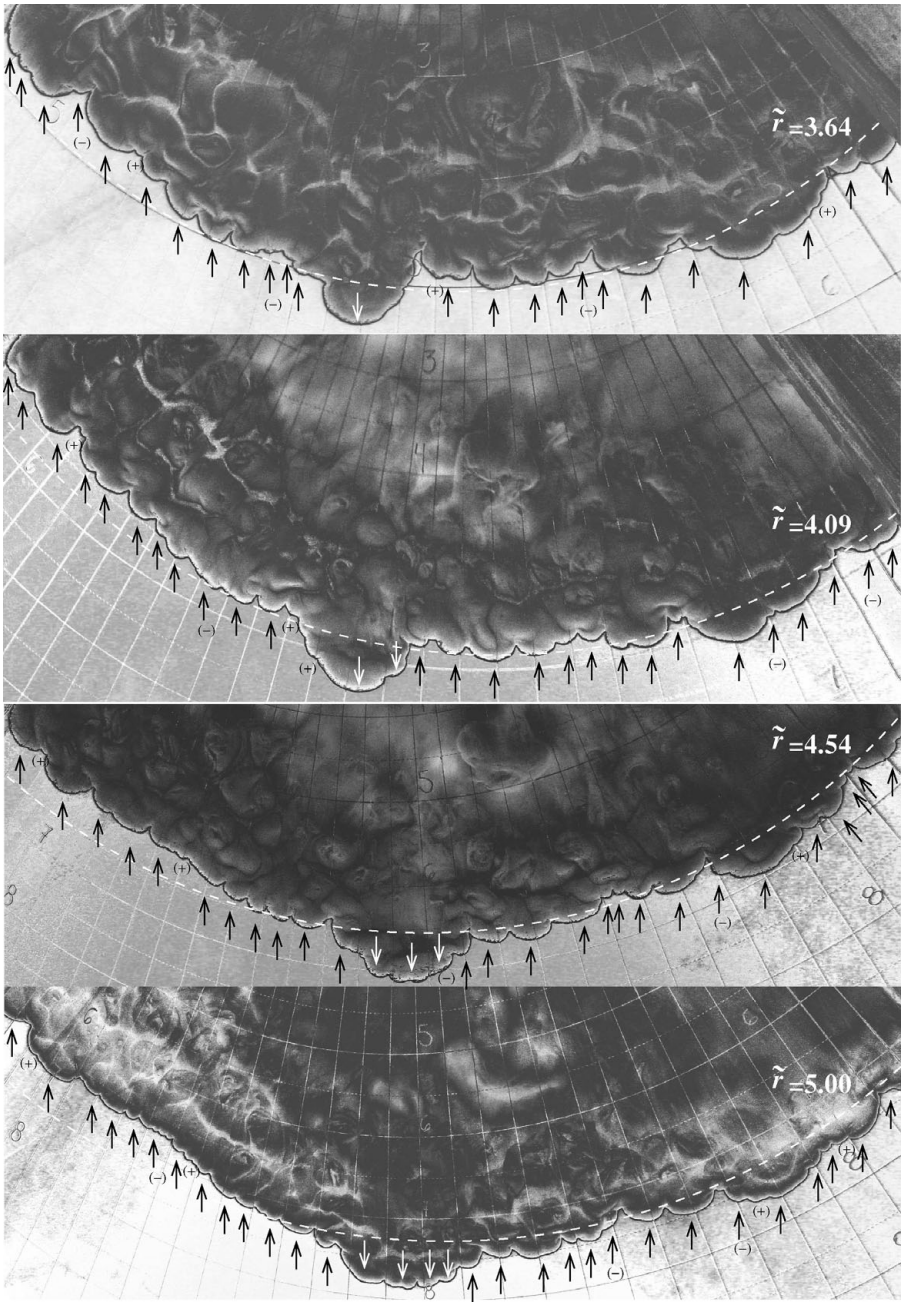

FIGURE 14. Lobes and clefts from an experiment for $Re = 8950$ and $Sc = 700$. Each frame shows the entire front in the experiment which extends over a circular section of $\pi/2$. From top to bottom, the frames correspond to time instances when the front is locate at $\tilde{r} = 3.6$, 4.1, 4.5 and 5.0, respectively. Through postprocessing the lobe-and-cleft pattern has been demarcated in the pictures. Each lobe is indicated with an arrow. Locations where a lobe is not clearly seen and it was not counted (but could have been counted) are marked (+). On the other hand, locations where a lobe has been counted but was not clearly seen are marked (−). In this way, an error can be estimated in the number of lobes counted.

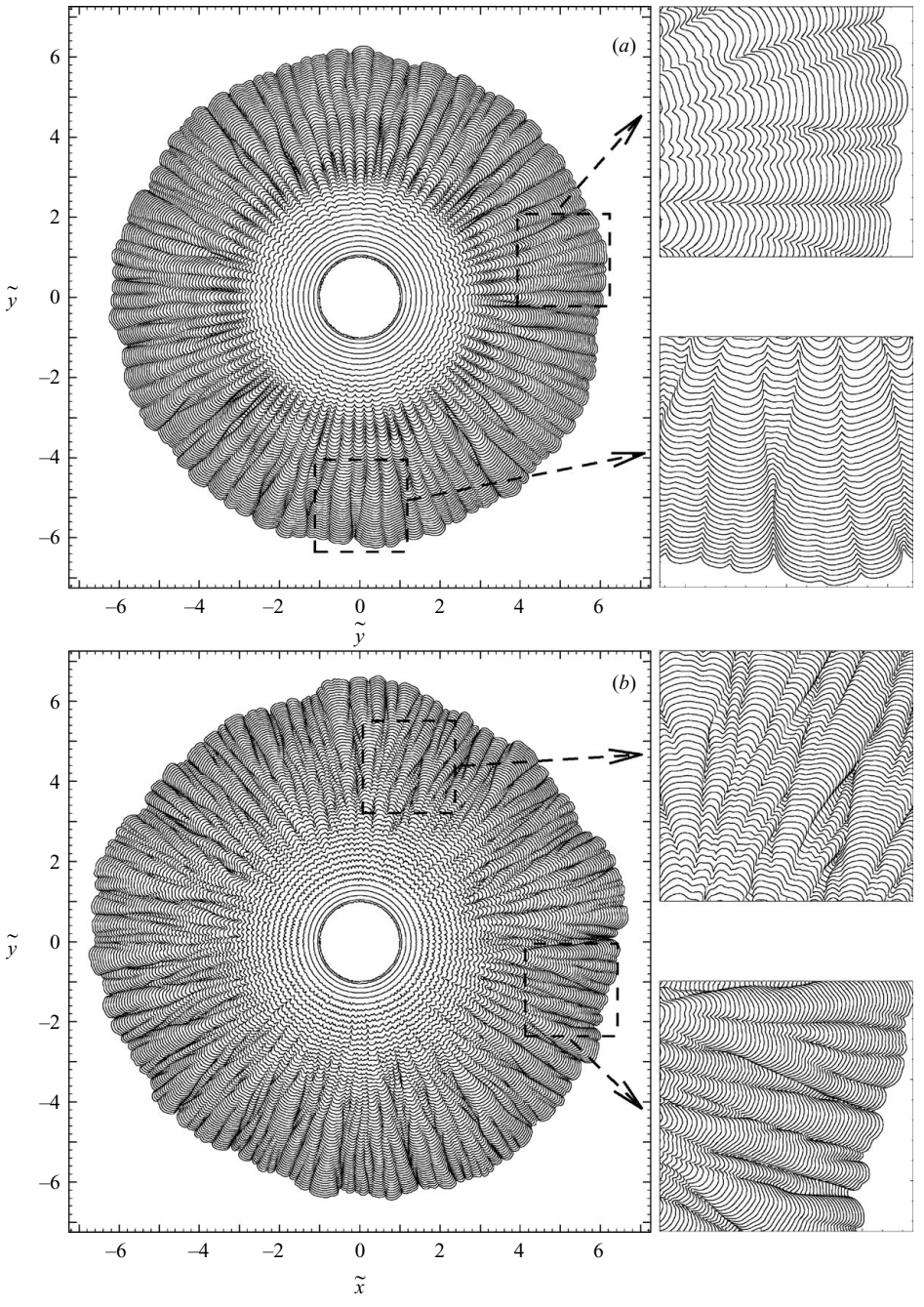

FIGURE 15. Composite picture of the front location over time. Front visualized by bottom contours of $\tilde{\rho} = 0.015$. The time separation between contours is $\Delta\tilde{t} = 0.354$. The details show several lobe splittings and merges. (*a*) $Re = 3450$, and (*b*) $Re = 8950$.

Figure 17 shows in detail the lobe-and-cleft pattern observed in the present experiments performed at $Re = 8950$. The front of the current is located at $\tilde{r} \simeq 6.5$. At this late time the height of the front and the concentration of potassium permanganate at the front have decreased enough to permit clear visualization of the lobes and

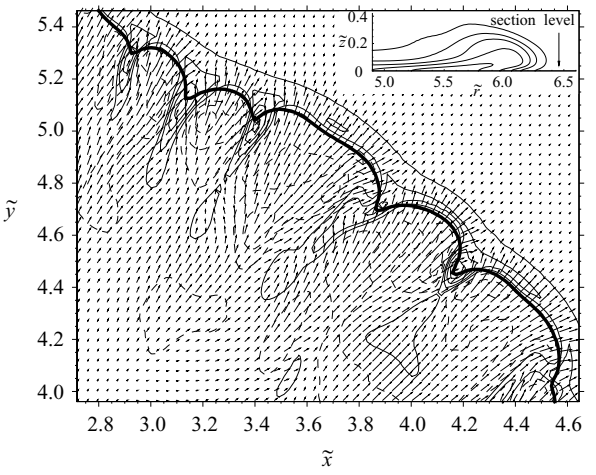

FIGURE 16. Near-bed flow at the front of the current for $Re = 3450$ at $\tilde{t} = 21$. The inset indicates the location of the section at $\tilde{z} = 0.04$ relative to the front. The front is visualized by the corresponding bottom density contour of $\tilde{\rho} = 0.015$ (thick solid line). The vector field shows the horizontal flow (velocity components $\tilde{u}_x$ and $\tilde{u}_y$) and the contour lines show the vertical flow (solid lines: positive $\tilde{u}_z$, and dashed lines: negative $\tilde{u}_z$). The vector field shows that the horizontal flow in the clefts is slower that in the lobes. It is clear also that there is an azimuthal flow component from the centre of the lobes into the clefts. The vertical flow is upward (solid contours) at the cleft locations and downward at the lobes location (dashed contours).

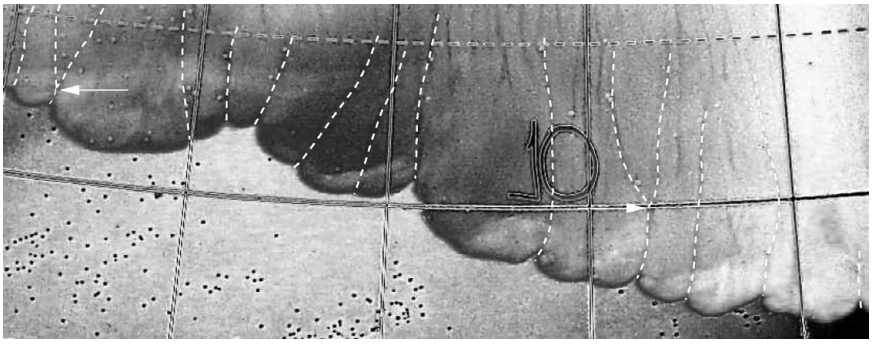

FIGURE 17. Detail of lobes and clefts from an experiment for $Re = 8950$ with $Sc = 700$. The front is located at $\tilde{r} \simeq 6.5$. At this time the concentration of potassium permanganate at the front has decreased enough to allow the visualization of cleft as streaks of fresh clear water trapped between the bottom boundary and the current in the near-front region. These streaks have been marked in the figure with dashed lines to help their visualization. Two mergers of clefts (marked with arrows) can be observed in the figure. Compare to figure 15.

clefts in the flow: long streaks of fresh clear water trapped between the bottom of the tank and the current can be clearly identified. These streaks mark the path traversed by the clefts and have been demarcated in the figure with dashed lines to help their visualization. The photograph not only provides information on the instantaneous structure of the front, but also captures the path etched by the clefts in the recent past. Thus the experimental photograph can be compared with the simulation results presented in figure 15 and the qualitative features are in agreement. For example,

Source	Re	$\tilde{t}$	$\overline{r}_F$	$\overline{u}_F$	$\overline{h}_H$	Re_F	N_{90}	$\tilde{\lambda}_l$	Phase
DNS	3450	3.9	2.4	0.36	0.4	499	16 ± 2	0.24	SP
DNS	3450	5.3	2.9	0.32	0.26	283	19.5 ± 2	0.24	IP
DNS	3450	7.1	3.4	0.26	0.33	291	20.25 ± 2	0.27	IP
DNS	3450	10.6	4.2	0.22	0.354	266	18 ± 2	0.36	IP
DNS	3450	14.1	5	0.2	0.32	221	19.5 ± 2	0.4	IP
DNS	3450	17.7	5.7	0.18	0.27	167	20.5 ± 2	0.44	VP
DNS	3450	21.2	6.3	0.15	0.25	129	22.25 ± 2	0.44	VP
DNS	3450	24.8	6.8	0.12	0.23	99	25 ± 2	0.42	VP
DNS	8950	1.8	1.7	0.41	0.3	1098	26.25 ± 3	0.1	SP
DNS	8950	3.5	2.4	0.38	0.36	1226	30.5 ± 3	0.12	SP
DNS	8950	7.1	3.6	0.29	0.29	774	25.25 ± 3	0.22	IP
DNS	8950	10.6	4.5	0.25	0.32	711	27 ± 3	0.26	IP
DNS	8950	14.1	5.3	0.22	0.28	542	27.25 ± 3	0.31	IP
DNS	8950	17.7	6	0.19	0.27	446	27.5 ± 3	0.34	VP
DNS	8950	20.9	6.6	0.14	0.25	301	28.25 ± 3	0.37	VP
EXP	8950		3.6				25 ± 3	0.23	
EXP	8950		4.1				28 ± 3	0.23	
EXP	8950		4.5				29 ± 3	0.24	
EXP	8950		5				31 ± 3	0.25	

TABLE 1. Quantitative information on the lobe-and-cleft structure. $\overline{r}_F$ is the mean radial location of the front, $\overline{u}_F$ is the front velocity, $\overline{h}_H$ is the current head height, $Re_F = Re\,\overline{h}_H\overline{u}_F$ is the local instantaneous Reynolds number of the front, N_{90} is the mean number of lobes observed within a 90° sector, and $\tilde{\lambda}_l = \pi\overline{r}_F/2N_{90}$ is the mean wavelength of the lobe. SP: slumping phase, IP: inertial phase, and VP: viscous phase.

what appears to be the initiation of new clefts and merger between existing clefts (marked with arrows) can be observed in the figure.

Quantitative information on the lobe-and-cleft structure for both $Re = 3450$ and 8950 is presented in table 1. At several selected time instances the mean radial location of the front ($\overline{r}_F$), the front velocity ($\overline{u}_F$), the current head height ($\overline{h}_H$), the local instantaneous Reynolds number of the front ($Re_F = Re\,\overline{h}_H\overline{u}_F$), the mean number of lobes observed within a 90° sector (N_{90}), and the mean wavelength of the lobe ($\tilde{\lambda}_l = \pi\overline{r}_F/2N_{90}$) are presented in the table. Also presented is the wavelength of the lobe extracted from the experiment (see figure 14). The counting of lobes on figures 14 and 15 is subject to some interpretation, especially at instances of incipient merger and splitting. In table 1 the number of lobes is therefore presented with an error. In addition to counting we have also computed both the Fourier spectrum and two-point correlation of the front location as a function of θ. Owing to the complex nature of the front, both the spectrum and correlation present a set of broad peaks. Nevertheless, their results are consistent with those obtained from simple counting.

The amplitude of disturbance introduced in the initial condition is the same at all Re, and from figure 15 it can be seen that at the higher Re the disturbance grows more rapidly and result in earlier formation of the distinct lobe-and-cleft structure. At both larger Re values the number of lobes initially goes through a brief period of adjustment where N_{90} first increases followed by some reduction. After this initial adjustment the number of lobes continus to increase with time. The increase is more prominent for $Re = 3450$, while at the higher $Re = 8950$ the increase is only modest. At $Re = 8950$ an increased competition for lobes to grow can be observed. For example,

one can observe in figure 15 instances where a new lobe is erased through merger before it reaches the mean size. Furthermore, careful observation of the details in figure 15(*b*) shows instances where out of a single lobe multiple smaller lobes are formed, but only one grows to the mean size. In contrast, at the lower $Re = 3450$ almost every lobe grows to reach the mean size of a lobe for that radial location as can be seen from figure 15(*a*). Typically, a lobe splits into two with both growing over time. There are, however, lobes merging as can be seen in the details of figure 15(*a*), but this process is less intense than in the case of $Re = 8950$.

Figure 18(*a*) shows the lobe size normalized by the current head height, $\overline{h}_H$, from the numerical simulations as a function of Re_F. The data for $Re = 3450$ are presented with solid symbols and those $Re = 8950$ with open symbols. The data are also separated by the corresponding phase of spreading. Also plotted in the figure are experimental data by Simpson (1972) for a planar current and the curve fit $7.4\,Re_F^{-0.39}$ suggested by him. The present simulation Re fall within the range studied by Simpson, but his measurements were only in the constant-velocity slumping regime. The present simulation results for the cylindrical currents during the different phases of spreading do not seem to follow a consistent power law. The wavelength of the lobe-and-cleft pattern in the slumping phase is in reasonable agreement with those by Simpson (1972). However, in the inertial and viscous phases our wavelength is substantially larger. The difference between planar and cylindrical currents could be the fact that the cylindrical current decays more rapidly due to its quadratic spreading.

It is of interest to compare the present experimental results with those from the simulation at $Re = 8950$. However, in the experiment only top view visualizations were performed and as a result the instantaneous height of the current's head is not available. We, thus, use an equivalent current height as obtained from a simple box-model-based mass conservation $\overline{h}_r = (\overline{r}_0/\overline{r})^2$. In figure 18(*b*) we present the wavelength of the lobe-and-cleft pattern normalized by $\overline{h}_r$ as a function of $Re_r = Re\overline{u}_F\,\overline{h}_r$. Both the computational and experimental results are plotted and the agreement is very good. Interestingly, with this scaling the variation between the different phases of spreading is smaller.

3.7. *Turbulent structures*

The complex three-dimensional vortical structure of the current is not entirely apparent in the density isosurface presented in figure 4. The corresponding isosurface of swirling strength at the later three times is shown in figure 19: the three-dimensional vortical structure of the high-Re current is extracted well by $\tilde{\lambda}_{ci}$. The root-mean-square swirling strength within the vortical region at the three different times is 1.05, 0.93 and 0.32, respectively. The isosurface of $\tilde{\lambda}_{ci} = 2.12$ is plotted in figure 19 for the first two time instances of $\tilde{t} = 7$ and 14. For $\tilde{t} = 21$ the isosurface of $\tilde{\lambda}_{ci} = 0.35$ is plotted. Thus, the figure captures only the intense vortical regions of the flow for all the times displayed. At the first instance shown in figure 19, the strong vortical structures extracted near the head of the current are associated with the Kelvin–Helmholtz vortex rings A1 and A5. The effect of lobes and clefts on the vortical structure can be clearly observed. Two other rings of intense turbulence can be seen. The one centred around $\tilde{r} \approx 1.75$ is associated with the merged vortex ring A2+A3. The final weaker ring of turbulent structures is associated with vortex ring A4. By $\tilde{t} = 14$, all except the vortex ring associated with the front of the current have already decayed and any turbulence associated with them is no longer captured by $\tilde{\lambda}_{ci} = 2.12$. However, this is an artifact of the relatively high threshold of 2.12 set for visualization. In figure 19 for $\tilde{t} = 21$ the isosurface of $\tilde{\lambda}_{ci} = 0.35$ shows that active turbulence is still present.

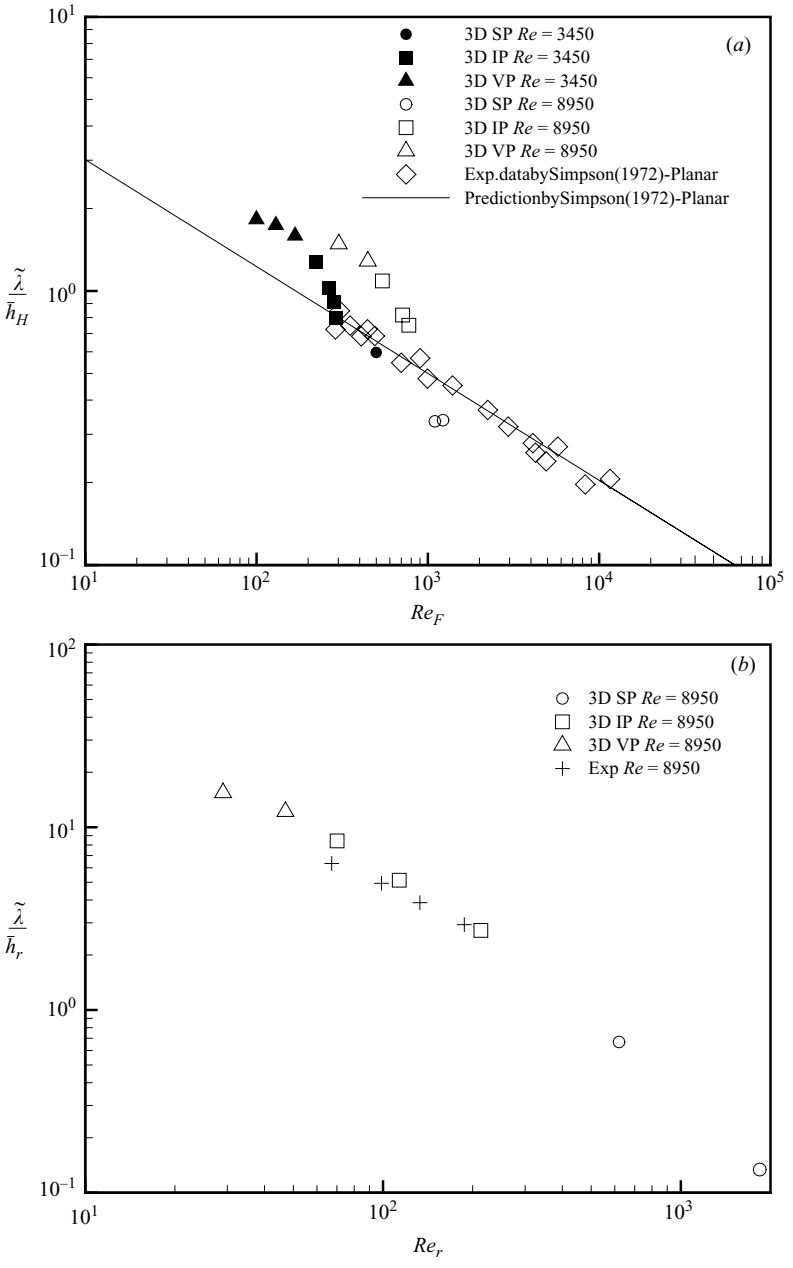

FIGURE 18. Lobe size for cylindrical currents as a function of local *Re*. (*a*) Lobe size normalized by current head height, $\bar{h}_H$, as a function of $Re_F = Re\bar{u}_F\,\bar{h}_H$. Also in this plot are the experimental data for planar currents by Simpson (1972) and the best fit to his data. (*b*) Lobe size normalized by current head height, $\bar{h}_r = (\bar{r}_0/\bar{r})^2$, as a function of $Re_r = Re\bar{u}_F\,\bar{h}_r$. Also in this plot are data from figure 14 for the experiment with $Re = 8950$. The data from numerical simulations is differentiated by the corresponding phase of spreading. SP: slumping phase, IP: inertial phase, and VP: viscous phase.

A low level of turbulence can be observed behind the vortex rings. In addition we observe turbulence associated with a second vortex ring (A2+A3) located at $\tilde{r} \approx 3.75$ and close to the origin.

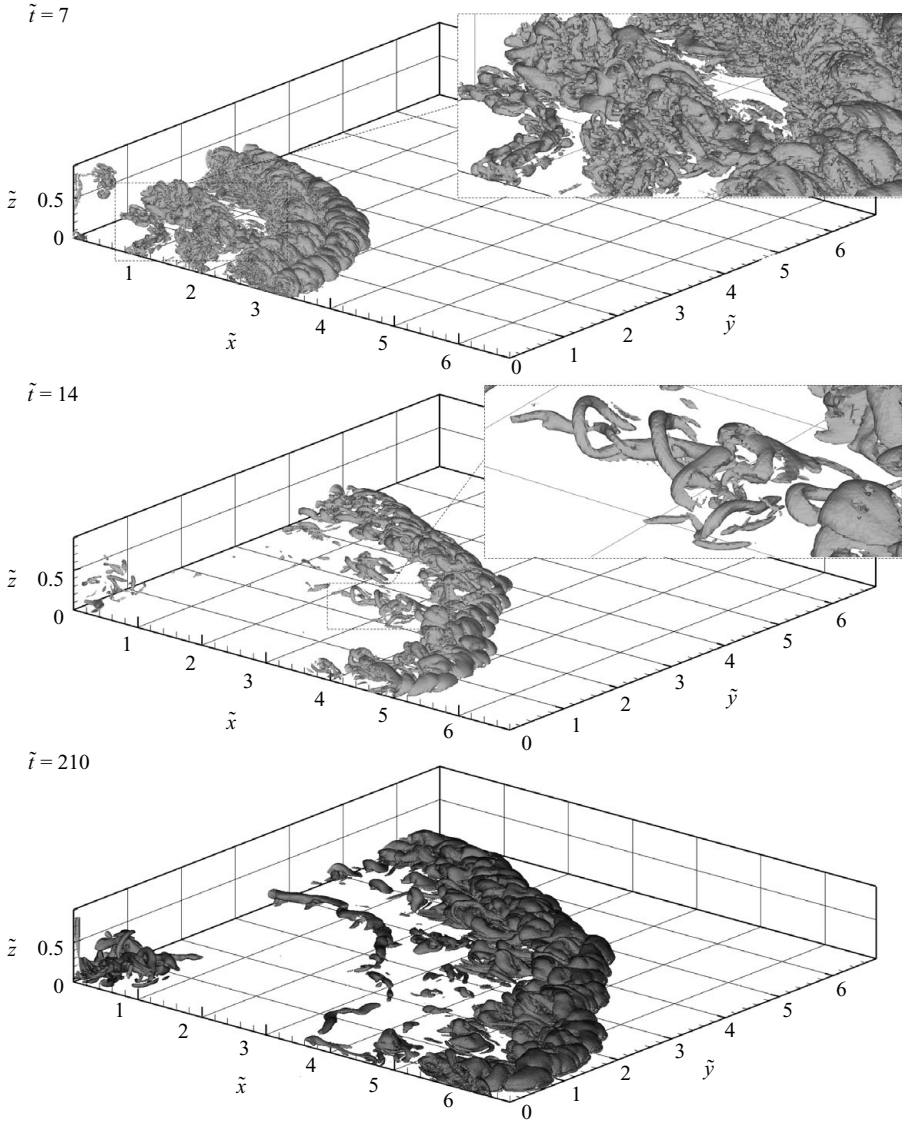

FIGURE 19. Flow structures visualized by an isosurface of $\tilde{\lambda}_{ci}$. For $\tilde{t} = 7$ and 14 the isosurface of $\tilde{\lambda}_{ci} = 2.12$ is shown, while for $\tilde{t} = 21$ the isosurface of $\tilde{\lambda}_{ci} = 0.35$ is shown. The insets show detailed views. The inset in frame for $\tilde{t} = 14$ shows a train of asymmetric hairpin vortices that have formed behind the front.

Apart from the vortex rings and the lobe-and-cleft structure, the turbulent region of the flow behind the head is dominated by inclined vortical structures and several hairpin vortices can be observed (see for example the inset for $\tilde{t} = 14$). These structures are similar to those observer in a turbulent wall layer, where the vortical structures are tilted from the wall in the flow direction. In the case of a cylindrical gravity current, the flow induced is directed radially out. However, in a frame of reference moving with the front, the flow within the current is radially inward, which explains the observed orientation of the vortical structures within the current. Similar trains of inclined vortical structures were observed for the case of planar gravity currents

as well (Cantero *et al.* 2007). The difference, however, is that at the present Re in the planar current the region of turbulence extended over a large portion of the body of the current, while in the cylindrical case turbulence is limited to only vortex rings and the head of the current. The net effect of the vortical structures on the concentration (density) field is seen in figure 4.

3.8. *Subcritical vs. supercritical flow*

As seen in figure 6 the presence of vortex rings gives rise to significant local variation in the height and velocity of the current, inducing regions of subcritical and supercritical flow. A local Froude number of the flow can be defined as

$$Fr = \frac{\overline{u}(r)}{\sqrt{g'\,\overline{h}(r)}} \tag{3.13}$$

where the local height and velocity of the current are defined as

$$\overline{h}(r) = \int_0^H \left(\frac{1}{2\pi} \int_0^{2\pi} \frac{\rho(r,\theta,z) - \rho_0}{\rho_1 - \rho_0}\, \mathrm{d}\theta \right) \mathrm{d}z, \tag{3.14}$$

$$\overline{u}(r) = \frac{\displaystyle\int_0^H \left(\frac{1}{2\pi} \int_0^{2\pi} u(r,\theta,z) \frac{\rho(r,\theta,z) - \rho_0}{\rho_1 - \rho_0}\, \mathrm{d}\theta \right) \mathrm{d}z}{\displaystyle\int_0^H \left(\frac{1}{2\pi} \int_0^{2\pi} \frac{\rho(r,\theta,z) - \rho_0}{\rho_1 - \rho_0}\, \mathrm{d}\theta \right) \mathrm{d}z}. \tag{3.15}$$

It must be stressed that Fr is not the dimensionless front velocity, but provides a dimensionless measure of the local fluid velocity compared to that of the local speed of wave propagation. The above definitions of $\overline{u}$, $\overline{h}$ and Fr are not unique, and some caution is required in interpreting regions of $Fr > 1$ and $Fr < 1$ as supercritical or subcritical flow regions. Nevertheless, we observe that with the above definition of Fr, the head of the current consistently remains very close to critical which is indicative of a reasonable choice of scales.

Figure 20 shows $\overline{u}$ (solid line), $\overline{h}$ (dashed line) and Fr (dash-dot line) as a function of $\tilde{r}$ at several times from $\tilde{t} = 1.77$ to 21. The current presents a well-defined front, where $\overline{h}$ reaches its maximum, and a shallower body and tail. Some of these features are well-captured by shallow water models (Ungarish & Zemach 2005; Ungarish 2007) even though they cannot describe the formation and evolution of Kelvin–Helmholtz vortex rings. At the front of the current $\overline{u}$ and $\overline{h}$ approach zero; however, the decrease of $\overline{u}$ is slower than that of $\overline{h}$ and, as a result, the Fr rapidly increases. The supercritical nature of the flow at the front is consistent with the front-like character ('shock') of the current. The current at all times has an extended shallow body behind the raised head. At early times during the slumping phase of spreading ($\tilde{t} \lesssim 5.5$) several undulations are present along the body of the current. It can be observed that $\overline{h}$ increases at the location of the vortex rings, while $\overline{u}$ shows local peaks in regions in between the vortex rings, where the current is shallower. The combined effect creates large-amplitude fluctuations in Fr. At later times, as the vortex rings dissipate during the inertial and viscous phases, the undulations in $\overline{u}$, $\overline{h}$ and Fr diminish.

During the slumping phase of spreading ($\tilde{t} \lesssim 5.5$), $Fr > 1$ over the entire length of the current. At intermediate times, during the inertial phase of spreading ($5.5 \lesssim \tilde{t} \lesssim 17$), $Fr > 1$ only in the region between the vortex rings A1 and A5. Eventually, as the current decays during the viscous phase, the Froude number becomes subcritical ($Fr < 1$) over the entire length of the current, except at the head where the critical value is maintained at all times. When the front is located at about $\tilde{r} = 3.5$, the

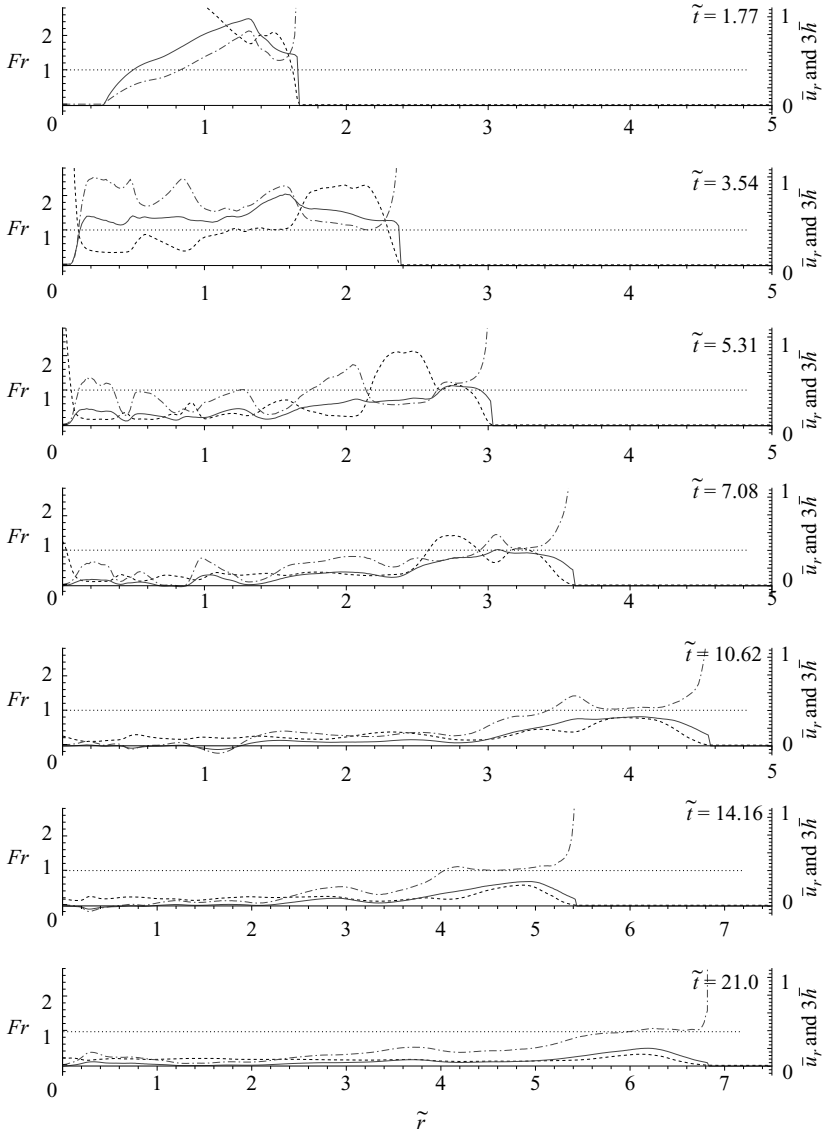

FIGURE 20. Evolution of depth-averaged variables for $Re = 8950$. Solid line: $\overline{u}$, dashed line: $\overline{h}$, and dash-dot line: Fr. The dotted line indicates $Fr = 1$. Observe that $Fr \sim 1$ at the front location for all time. On the body of the current Fr transitions from larger than 1 to smaller than 1 at $\tilde{t} \sim 6$.

flow presents an elevated front, which produces a region of higher pressure over $2.5 < \tilde{r} < 3.5$. The resulting lateral pressure gradient enhances the driving force to accelerate the front radially outward, but also applies a retarding force to the shallow body trailing the head of the current. This interaction induces the separation of the head from the body of the current, which is indicated by the dip in the current height at $\tilde{r} \simeq 2.9$ at $\tilde{t} = 10.6$. Although subtle, this dip in the height persists at all times, and can be visualized in the three-dimensional figures as a circular wave at $\tilde{r} \simeq 4$ (compare figures 4 and 20). It is interesting to note that there are instances where

the pressure gradient points radially inward so that the velocity of the current and correspondingly the Froude number become negative.

4. Summary and conclusions

In this work we present highly resolved three-dimensional simulations of cylindrical density currents performed at three different *Re* of 895, 3450, and 8950 with the objective of addressing the structure and dynamics of cylindrical density currents. The simulations have been conducted with a de-aliased spectral code, which captures all relevant length scales present in the flow.

As the front spreads, a shear layer forms between the heavy and the light fluids, inducing the formation of Kelvin–Helmholtz vortices at the interface. The dynamics of the interface is highly dependent on the *Re* of the flow. For the same aspect ratio of the initial release, we observe an increase of the growth rate and also of the formation frequency of the Kelvin–Helmholtz vortices with *Re*. At the lowest *Re* considered in this work only two vortex rings form, which remain axisymmetric during the entire duration of the simulation. The interface stays smooth and nearly horizontal behind the front. At the larger two *Re* considered four and five vortex rings form, respectively, which are destabilized in the azimuthal direction and eventually break up into smaller scale turbulence. In these cases the interface is very irregular with large undulations and evolves more dynamically than in the lowest *Re* case.

The roll-up process of the interface into coherent vortices proceeds only during the initial slumping phase of spreading. Along with the formation of Kelvin–Helmholtz vortices at the interface, a series of counter-rotating vortices forms at the bottom boundary and their eventual interaction results in the lift-up and retardation of the original Kelvin–Helmholtz vortex ring. The retardation of the leading vortex ring results in the detachment of the head of the current and in the formation of an additional vortex ring in the front.

An important consequence of the vortex formation is that the local height and velocity of propagation of the current vary strongly along its length, and so does the local Froude number. A local Froude number can be defined in term of depth-averaged variables to discriminate between regions of sub- and supercritical flow. Interestingly, the local Froude number remains close to critical for all time at the head of the current. Some of the features shown on the depth-averaged-variables plots are captured well by shallow water models (Ungarish 2007). In particular, shallow water models capture better the front velocity than highly resolved two-dimensional simulations (Cantero *et al.* 2007).

Regions of turbulence in the flow are associated with the breakup of the vortex rings. In the cylindrical geometry the behaviour of the Kelvin–Helmholtz vortices is somewhat different from that in the planar configuration. As the vortex rings propagate radially out, they are inherently stretched along the azimuthal direction, which is expected to provide additional stability. Small disturbances introduced into the initial condition result in small-amplitude bending and twisting perturbations of the vortex rings. At $Re = 895$ these disturbances decay and the vortex rings remain structurally stable. At the higher two Reynolds numbers of 3450 and 8950, the instability grows and the vortex rings break up and take a three-dimensional structure. The stability of the Kelvin–Helmholtz vortices in the planar case at these *Re* is qualitatively similar. This suggests that the stretching of the vortex rings in the cylindrical case does not stabilize the structures sufficiently to greatly alter the critical *Re* for the onset of three-dimensionality. In both the full-depth planar and cylindrical

releases this critical *Re* is between 895 and 3450. Further investigation is required to narrow the critical *Re* range and clarify the influence of circumferential stretching. The growth of instability results in the lobe-and-cleft structure of the head and in the breakdown of the vortex rings into coherent vortical structures. These regions are populated with trains of hairpin vortices tilted toward the axis. Similar findings have been reported by Cantero *et al.* (2007) for planar currents; however, in that case the hairpin vortices are distributed evenly over the head and body of the current.

At the larger two *Re*, a clear pattern of lobes and clefts develops originally at the lower part of the leading front, but very rapidly extends to the upper and rear part of the front. Once formed, the pattern evolves very dynamically, presenting merging of clefts and splitting of lobes into new ones. The process is similar at both *Re*; however, with increasing *Re* the flow is characterized by smaller scales. The wavelength of the lobes grows with time as the front spreads and the local *Re* of the flow decreases. This is consistent with previous studies on planar currents that show that the most unstable wavelength decreases with *Re* (Härtel *et al.* 2000*a*). However, for cylindrical currents the number of lobes is maintained over time and the increase in wavelength is associated with the increase in circumferential length of the current.

A laboratory experiment was performed for the case of salt water spreading in quiescent fresh water. The Schmidt number in the experiment was 700, while in the numerical simulations $Sc = 1$. Although the setting of the experiment was not exactly as in the simulations, the front velocity, the wavelength of the lobe-and-cleft structures and their temporal dynamics computed in the numerical simulations are in good agreement with the experimental observations. The general agreement implies that the dynamics of the front and its propagation are primarily dictated by *Re* and the size of the release and are not greatly influenced by *Sc* (Härtel *et al.* 2000*b*; Cantero *et al.* 2006).

We gratefully acknowledge the support of the Coastal Geosciences Program of the US Office of Naval Research (grant N00014-93-1-0044), National Science Foundation (grant EAR0609712), the Chicago District of the US Army Corps of Engineers, and the Metropolitan Water Reclamation District of Greater Chicago. Support from the National Center for Supercomputing Applications (NCSA) at the University of Illinois at Urbana-Champaign (UIUC) is also acknowledged. Mariano Cantero was supported by a Graduate Student Fellowship from the Computational Science and Engineering Program at UIUC. Experiment were performed with the help and suggestions of Dr. Carlos M. García. Dr. James Ferry collaborated in the early stages of the computations. Computer time was partially provided by Dr. Nahil Sobh and Dr. Fady Najjar. Dr. Gregory Bauer from NCSA helped to solve memory issues to run the larger simulation. Dr. David Bock from NCSA produced visualizations of the larger simulation.

REFERENCES

Alahyari, A. & Longmire, E. 1996 Development and structure of a gravity current head. *Exps. Fluids* **20**, 410–416.

Allen, J. 1971 Mixing at turbidity current heads, and its geological implications. *J. Sediment. Petrol.* **41**, 97–113.

Allen, J. 1985 *Principles of Physical Sedimentology*. George Allen and Unwin Ltd.

Bonnecaze, R., Hallworth, M., Huppert, H. & Lister, J. 1995 Axisymmetric particle-driven gravity currents. *J. Fluid Mech.* **294**, 93–121.

Cantero, M., Balachandar, S., García, M. & Ferry, J. 2006 Direct numerical simulations of planar and cyindrical density currents. *Trans. ASME: J. Appl. Mech.* **73**, 923–930.

Cantero, M., Lee, J. R., Balachandar, S. & García, M. 2007 On the front velocity of gravity currents. *J. Fluid Mech.* **586**, 1–39.

Chakraborty, P., Balachandar, S. & Adrian, R. 2005 On the relationships between local vortex identification schemes. *J. Fluid Mech.* **535**, 189–214.

Fannelop, T. & Waldman, G. 1971 The dynamics of oil slicks – or 'creeping crude. *AIAAJ* **41**, 1–10.

Fay, J. 1969 The spreads of oil slicks on a calm sea. In *Oils in the Sea* (ed. D. P. Hoult), pp. 53–63. Plenum.

García, M. & Parsons, J. 1996 Mixing at the front of gravity currents. *Dyn. Atmosp. Oceans* **24**, 197–205.

Hallworth, M., Huppert, H., Phillips, J. & Sparks, R. 1996 Entrainment into two-dimensional and axisymmetric turbulent gravity currents. *J. Fluid Mech.* **308**, 289–311.

Hallworth, M., Huppert, H. & Ungarish, M. 2001 Axisymmetric gravity currents in a rotating system: experimental and numerical investigations. *J. Fluid Mech.* **447**, 1–29.

Härtel, C., Carlsson, F. & Thunblom, M. 2000*a* Analysis and direct numerical simulation of the flow at a gravity-current head. Part 2. The lobe-and-cleft instability. *J. Fluid Mech.* **418**, 213–229.

Härtel, C., Meiburg, E. & Necker, F. 2000*b* Analysis and direct numerical simulation of the flow at a gravity-current head. Part 1. Flow topology and front speed for slip and no-slip boundaries. *J. Fluid Mech.* **418**, 189–212.

Hoult, D. 1972 Oil spreading in the sea. *Annu. Rev. Fluid Mech.* **4**, 341–368.

Huppert, H. 1982 The propagation of two-dimensional and axisymmetric viscous gravity currents over a rigid horizontal surface. *J. Fluid Mech.* **121**, 43–58.

Huppert, H. & Simpson, J. 1980 The slumping of gravity currents. *J. Fluid Mech.* **99**, 785–799.

Lee, B. & Wilhelmson, R. 1997*a* The numerical simulation of non-supercell tornadogenesis. Part I: Initiation and evolution of pretornadic misocyclone circulation along a dry outflow boundary. *J. Atmos. Sci.* **54**, 32–60.

Lee, B. & Wilhelmson, R. 1997*b* The numerical simulation of non-supercell tornadogenesis. Part II: Evolution of a family of tornadoes along a weak outflow boundary. *J. Atmos. Sci.* **54**, 2387–2415.

Marino, B., Thomas, L. & Linden, P. 2005 The front condition for gravity currents. *J. Fluid Mech.* **536**, 49–78.

Martin, J. & Moyce, W. 1952 Part V. An experimental study of the collapse of fluid columns on a rigid horizontal bottom, in a medium of lower, but comparable, density. *Phil. Trans. R. Soc. Lond.* A **244**, 325–334.

Necker, F., Härtel, C., Kleiser, L. & Meiburg, E. 2002 High-resolution simulations of particle-driven gravity currents. *Intl J. Multiphase Flow* **28**, 279–300.

Özgökmen, T., Fischer, P., Duan, J. & Iliescu, T. 2004 Three-dimensional turbulent bottom density currents from a high-order nonhydrostatic spectral element model. *J. Phys. Oceanogr.* **34**, 2006–2026.

Parsons, J. & García, M. 1998 Similarity of gravity current fronts. *Phys. Fluids* **10**, 3209–3213.

Patterson, M., Simpson, J., Dalziel, S. & van Heijst, G. 2006 Vortical motion in the head of an axisymmetric gravity current. *Phys. Fluids* **18** (4), 046601.

Rottman, J. & Simpson, J. 1983 Gravity currents produced by instantaneous releases of a heavy fluid in a rectangular channel. *J. Fluid Mech.* **135**, 95–110.

Simpson, J. 1972 Effects of the lower boundary on the head of a gravity current. *J. Fluid Mech.* **53** (4), 759–768.

Simpson, J. 1997 *Gravity Currents*, 2nd edn. Cambridge University Press.

Simpson, J. & Britter, R. 1979 The dynamics of the head of a gravity current advancing over a horizontal surface. *J. Fliud Mech.* **94**, 477–495.

Ungarish, M. 2007 Axisymmetric gravity currents at high reynolds numbers: On the quality of shallow-water modeling of experimental observations. *Phys. Fluids* **19**, 036602.

Ungarish, M. & Zemach, T. 2005 On the slumping of high reynolds number gravity currents in two-dimensional and axisymmetric configurations. *Eur. J. Mech.* B/*Fluids* **24**, 71–90.

Wu, J., Ma, H. & Zhou, M. 2006 *Vorticity and Vortex Dynamics*. Springer.

Zhou, J., Adrian, R., Balachandar, S. & Kendall, T. 1999 Mech. for generating coherent packets of hairpin vortices. *J. Fluid Mech.* **387**, 353–396.